Published in final edited form as:
Biomech Model Mechanobiol. 2013 October ; 12(5): 1053–1071. doi:10.1007/s10237-012-0462-z.

Mechanics of the mitral valve:

A critical review, an in vivo parameter identification, and the effect of prestrain

Manuel K. Rausch,
Department of Mechanical Engineering, Stanford University, 496 Lomita Mall, Stanford, CA 94305, USA

Nele Famaey,
Department of Mechanical Engineering, KU Leuven, Celestijnenlaan 300, 3001 Leuven, Belgium

Tyler O'Brien Shultz,
Department of Mechanical Engineering, Stanford University, 496 Lomita Mall, Stanford, CA 94305, USA

Wolfgang Bothe,
Department of Cardiothoracic Surgery, Friedrich Schiller University, Jena, Germany

D. Craig Miller, and
Department of Thoracic Surgery, Stanford University, 300 Pasteur Dr, Stanford, CA 94305, USA

Ellen Kuhl
Departments of Mechanical Engineering, Bioengineering, and Cardiothoracic Surgery, Stanford University, 496 Lomita Mall, Stanford, CA 94305, USA, ekuhl@stanford.edu, tel.: +1.650.450.0855, fax: +1.650.725.1587

Manuel K. Rausch: mkrausch@stanford.edu; Nele Famaey: nele.famaey@mech.kuleuven.be; Tyler O'Brien Shultz: tshultz@stanford.edu; Wolfgang Bothe: wbothe@googlemail.com; D. Craig Miller: dcm@stanford.edu

Abstract

Alterations in mitral valve mechanics are classical indicators of valvular heart disease, such as mitral valve prolapse, mitral regurgitation, and mitral stenosis. Computational modeling is a powerful technique to quantify these alterations, to explore mitral valve physiology and pathology, and to classify the impact of novel treatment strategies. The selection of the appropriate constitutive model and the choice of its material parameters are paramount to the success of these models. However, the in vivo parameters values for these models are unknown. Here we identify the in vivo material parameters for three common hyperelastic models for mitral valve tissue, an isotropic one and two anisotropic ones, using an inverse finite element approach. We demonstrate that the two anisotropic models provide an excellent fit to the in vivo data, with local displacement errors in the sub-millimeter range. In a complementary sensitivity analysis, we show that the identified parameter values are highly sensitive to prestrain, with some parameters varying up to four orders of magnitude. For the coupled anisotropic model, the stiffness varied from 119,021kPa at 0% prestrain via 36kPa at 30% prestrain to 9kPa at 60% prestrain. These results may, at least in part, explain the discrepancy between previously reported ex vivo and in vivo measurements of mitral leaflet stiffness. We believe that our study provides valuable guidelines for modeling mitral valve mechanics, selecting appropriate constitutive models, and choosing physiologically meaningful parameter values. Future studies will be necessary to experimentally and computationally investigate prestrain, to verify its existence, to quantify its magnitude, and to clarify its role in mitral valve mechanics.

Correspondence to: Ellen Kuhl.

Keywords

Mitral valve; Constitutive modeling; Inverse finite element analysis; Parameter identification; Prestrain; Sensitivity analysis

1 Introduction

Its prominent role in the heart has made the mitral valve one of the most studied elements of the cardiovascular system. Within the past two decades, the finite element method has gained an increasing popularity in supporting these investigations. Finite element modeling has not only been successful when studying mitral valve physiology [11,50] and pathology [27,28], but also when evaluating novel surgical techniques [49,58] and medical devices [32,59].

One of the most crucial aspects of modeling mitral valve mechanics is the selection of appropriate constitutive models, along with the identification of their parameter values. Formulating a constitutive model for mitral valve tissue bears a number of challenges, some of which are unique to biological soft tissues. Exposed to large pressure gradients, the mitral leaflet undergoes large deformations and is subject to finite strains [44,53]. Optimized to sustain physiological loads, the valvular microstructure displays significant directional, regional, and transmembrane variations [24]. Supported by a collagenous extracellular matrix, the constitutive response is highly nonlinear, associated with the characteristic stress locking of collagen [15,16,30]. Equipped with active substructures, the mitral leaflet might be capable to actively contract [21,22]. Responding to mechanical stimuli, the living mitral valve tissue continuously turns over, adapts, grows, and remodels [6,7,47]. Exposed to a living environment, the constitutive response might be hugely sensitive to prestrain [2,57]. In summary, we are looking at an anisotropic, hyperelastic, strain-stiffening, actively contracting, adaptively growing, prestrained living material.

Since the first constitutive models for valvular tissue have been proposed two decades ago [25,49], various modifications and refinements have been suggested to accurately characterize the mitral valve leaflet. While clinical studies commonly still assume the mitral leaflet to behave linearly elastic [39,61], the trend clearly goes toward modeling it as an anisotropic hyperelastic material. One of the first and most prominent models introduced exclusively for mitral leaflet tissue is an invariant based hyperelastic model, which was calibrated in terms of a series of systematic ex vivo biaxial experiments [34]. Recent advancements have enhanced its robustness and numerical efficiency within a finite element setting [40] and incorporated active leaflet contraction [55]. Several other groups have recently proposed alternative hyperelastic models for mitral leaflet tissue [10,60]. Yet, to date, all hyperelastic models have only been calibrated using ex vivo experiments, and little is known about their parameter values in an in vivo setting.

Recently, in a series of systematic studies, our group has adopted inverse finite element modeling in conjunction with biplane videofluorscopic imaging to identify the material parameters of an anisotropic linear elastic model for mitral leaflet tissue [21,22]. The calibrated parameter sets suggest that the anterior mitral leaflet behaves several orders of magnitude stiffer in vivo than in vitro. These findings are significant in that predictive models, based on inaccurate material parameters, would significantly underestimate leaflet stress. Here, we adopt an inverse finite element approach to identify the in vivo material parameters for three prominent hyperelastic constitutive models. After a preliminary sensitivity analysis with a simple isotropic model, we explore the performance of two more

advanced anisotropic models for leaflet tissue [18,34], and investigate the effect of prestrain on their material parameter values.

2 Background

Modeling the mitral valve demands a sound understanding of its function, structure, and composition. In the following section we briefly review the basic knowledge related to these three aspects before proceeding with our study.

2.1 Mitral Valve Function

The mitral valve is one of four valves that ensure unidirectional blood flow through the heart. It is situated between the left ventricle and the left atrium and essentially serves as a check valve. In this role, it prevents blood from flowing back from the left ventricle into the left atrium during the contractile phase [8,37]. The mitral valve apparatus that enables this functionality consists of three elements: the anterior and posterior mitral leaflets, two collagenous tissue flaps that coapt under pressure and seal the mitral valve orifice to prevent leakage; the mitral annulus, the hinge region between the mitral leaflets and the surrounding myocardial tissue; and the subvalvular apparatus including the chordae tendineae and the papillary muscles, see Figure 1. During the onset of systole, when the heart muscle contracts, the intra-ventricular pressure rises, creating a pressure difference across the mitral leaflets. This pressure gradient is the primary driving force for mitral valve closure. Once the leaflets contact and form a close coaptation line, the subvalvular apparatus, through the chordae tendineae attached to the free leaflet edges, the leaflet belly, and close to the annulus, restrict leaflet motion and prevent their prolapse into the left atrium. A well-coordinated and sensitive interplay between all members of the mitral valve apparatus ensures mitral valve function in the healthy heart. Disease or damage to any of these components may result in improper coaptation and enable backflow of blood from the left ventricle into the left atrium [5,8].

2.2 Mitral Leaflet Structure and Function

Most of today's understanding of mitral leaflet structure and function is based on ex vivo testing of explanted leaflet tissue [15,33], on ex vivo testing of functional valves in pulsatile left heart simulators [38,43], on in vivo testing in large animals [2,54], and on clinical studies in patients [20,39]. Small angle light scattering has allowed to decipher the complex microstructure of mitral leaflet tissue. Its extracellular matrix is composed of a highly organized collagen network, spanning circumferentially across the anterior leaflet [9]. This fiber distribution may display significant heterogeneities throughout the thickness direction [26]. The first series of uniaxial tension tests on explanted leaflet tissue revealed a pronounced nonlinear stress-strain behavior with varying stiffnesses in fiber and cross-fiber directions [24]. The follow-up series of quasi-static planar biaxial tests produced a coherent data base, which is commonly used today to calibrate constitutive models of mitral leaflet tissue [33]. In viscoelastic studies of a similar biaxial setup, mitral leaflet tissue displayed no strain-rate dependence, no creep, and only minor hysteresis. However, mitral leaflet tissue did display a significant degree of relaxation [15,16,30]. In addition, recent studies in an infarct animal model [47] and in infarct patients [6,7] suggest that mitral leaflets may adaptively grow and remodel in response to environmental changes.

Ex vivo whole valve studies in pulsatile left heart simulators revealed mitral leaflet area strains of almost 100% under physiologic pressures [17,51]. Recent in vivo studies have observed mitral leaflet strains in the order of 10% to 20% throughout the cardiac cycle [44,52], a significantly smaller range than previously measured ex vivo. This controversy has initiated vivid discussions generating two complementary hypotheses: the theory of

active in vivo stiffening, supported by a sophisticated system of contractile elements found in mitral leaflets in the beating heart [19,22], and the theory of prestrain, supported by residual stresses reported in the physiological in vivo environment [2].

2.3 Mitral Leaflet Microstructure

Adult mitral leaflets possess three distinguishable layers throughout their thickness, the atrialis or spongiosa, the fibrosa, and the ventricularis. This three-layered core is lined on both surfaces by endothelial cells [35], which form a non-thrombogenic blood-tissue interface and regulate immune and inflammatory reactions. Of the three core layers, the fibrosa is the main load-bearing element, containing mainly thick, organized collagen fibers [26]. The atrialis contains a layer of loose connective tissue made of glyosaminoglycans and proteoglycans. The ventricularis is characterizaed primarily through elastin. Together, collagen, elastin, glyosaminoglycans, and proteoglycans form the extracellular matrix. The leaflet dry weight consists approximately of 60% collagen, 20% glyosaminoglycans, and 10% elastin [26]. The interior of the leaflet is populated sparsely by valvular interstitial cells, which are phenotypically similar to fibroblasts [36]. When stimulated pharmacologically or mechanically, valvular interstitial cells can undergo a transformation into myofibroblast-like cells, which are believed to be responsible for the remodeling capabilities of the tissue [6]. Recent studies have shown that valvular interstitial cells may possess smooth muscle cell-like properties [56].

3 Methods

3.1 Geometric Modeling

3.1.1 Data Acquisition—On cardiopulmonary bypass, we implanted 23 radiopaque tantalum markers onto the arterial surface of the anterior mitral leaflets and onto the mitral annuli of 57 male Dorsett sheep [3,29]. Sixteen markers were located in the anterior leaflet center and seven markers were located on the free edge and on the surrounding annulus [45], see Figure 2. In addition, we implanted one marker on each papillary muscle tip. After weaning the animals off cardiopulmonary bypass, we took biplane videofluoroscopic images of the markers in the beating heart at a 60Hz sampling frequency. Simultaneously, we recorded atrial, ventricular, and aortic pressures via catheter micromanometer pressure transducers. Using a semi-automatic digitization software, we obtained four-dimensional marker coordinates from biplane videofluoroscopy images throughout three complete cardiac cycles of all 57 sheep.

3.1.2 Temporal Interpolation—Since the sampling frequency was fixed while the heart rates varied from animal to animal, the number of data points per cardiac cycle was different for each animal. To create an average set of kinematic and hemodynamic data, we mapped all 57 data sets into four time intervals between end-diastole, end-isovolumic contraction, end-systole, end-isovolumic relaxation, and end-diastole of the next beat [44]. Within each interval, we performed a linear temporal interpolation of the marker coordinates and the hemodynamic data. Based on the different average lengths of the intervals, each interval was then resampled at six, fourteen, seven, and seventeen points, respectively. After resampling at these 40 points throughout the cardiac cycle and averaging over all animals, we obtained a temporally aligned average data set of four-dimensional marker coordinates and hemodynamic data [45,46], see Figure 4.

3.1.3 Spatial Interpolation—Based on the 23 averaged leaflet marker coordinates, see Figure 3A, we created a finite element discretization with 30 linear triangular shell elements for each time point of the simulation interval, see Figure 4. Using a custom-designed approximation subdivision algorithm [14], we then successively refined the mesh density to

120, 480, 1920, and 7680 elements, again for each time point, see Figure 3B–E. To determine the optimal mesh size [44], we performed a convergence study under physiologic pressures at end-systole where we compared the deflection of the central marker for different mesh densities. Based on this study, we selected the mesh with 1920 elements and 1017 nodes for all following analyses, see Figure 5.

3.1.4 Leaflet Microstructure—Mitral leaflet tissue is known to contain of a highly organized collagen network, spanning circumferentially across the entire mitral leaflet [9]. To confirm the collagen orientation in the sheep of our study, we performed a histological analysis of one representative ovine leaflet. We stained the explanted leaflet with Masson's Trichrome and then determined the collagen orientation microscopically, see Figure 6. Based on these observations and on reported fiber orientations in porcine mitral valves [9,41], we assigned regionally varying fiber directions to the mitral leaflet model. For each element, we chose the fiber orientation to be oriented orthogonal to the vector pointing from the saddle horn to the element centroid, see Figure 7.

3.2 Constitutive Modeling

We model mitral valve tissue as an incompressible, transversely isotropic, hyperelastic material. To set the stage, we first summarize the set of constitutive equations for this general class of materials. Then we derive three particular subclasses of models associated with three prominent constitutive models for mitral valve tissue [13,34].

We characterize leaflet deformation in terms of the deformation gradient $\boldsymbol{F} = \nabla\phi$, the spatial gradient of the deformation map ϕ, which maps material points from the reference to the current configuration. To account for the incompressible nature of soft biological tissues, we adopt the multiplicative decomposition of the deformation gradient into volumetric and isochoric parts,

$$\boldsymbol{F}=\boldsymbol{F}^{\mathrm{vol}}\cdot\overline{\boldsymbol{F}}\ \text{with}\ \boldsymbol{F}^{\mathrm{vol}}=J^{1/3}\boldsymbol{I}\ \text{and}\ \overline{\boldsymbol{F}}=J^{-1/3}\boldsymbol{F}, \quad (1)$$

implying that $\det(\overline{\boldsymbol{F}}) = 1$ and thus $J = \det(\boldsymbol{F}) = \det(\boldsymbol{F}^{\mathrm{vol}}) \geq 0$. To quantify leaflet deformation, we introduce the right Cauchy-Green deformation tensor $\boldsymbol{C}$ and its isochoric part $\overline{\boldsymbol{C}}$,

$$\boldsymbol{C}=\boldsymbol{F}^{\mathrm{t}}\cdot\boldsymbol{F}=J^{2/3}\overline{\boldsymbol{C}}\ \text{with}\ \overline{\boldsymbol{C}}=\overline{\boldsymbol{F}}^{\mathrm{t}}\cdot\overline{\boldsymbol{F}}. \quad (2)$$

To account for tissue microstructure, we assume that the leaflet is reinforced by a single family of collagen fibers introducing a transversely isotropic constitutive response. The associated unit vector $\boldsymbol{n}_0$ in the reference configuration defines the structural tensor

$$\boldsymbol{N}=\boldsymbol{n}_0\otimes\boldsymbol{n}_0 \quad \text{with} \quad \|\boldsymbol{n}_0\|=1. \quad (3)$$

From the possible set of three principal invariants and two pseudo-invariants characterizing a generic transversely isotropic constitutive behavior, we select the Jacobian J to account for the incompressible response, the first isochoric invariant $\bar{I}_1$ to account for the isotropic response, and the fourth isochoric invariant $\bar{I}_4$ to account for the anisotropic response,

$$\begin{array}{lll} J=\det(\boldsymbol{F}) & & \partial_{\boldsymbol{C}}J=\frac{1}{2}J\,\boldsymbol{C}^{-1} \\ \bar{I}_1=\overline{\boldsymbol{C}}:\boldsymbol{I} & \text{with} & \partial_{\overline{\boldsymbol{C}}}\bar{I}_1=\boldsymbol{I} \\ \bar{I}_4=\overline{\boldsymbol{C}}:\boldsymbol{N} & & \partial_{\overline{\boldsymbol{C}}}I_4=\boldsymbol{N}. \end{array} \quad (4)$$

We then adopt an incompressible, transversely isotropic, hyperelastic free energy function

$$\psi=\psi^{\mathrm{vol}}(J)+\bar{\psi}(\bar{I}_1,\bar{I}_4), \quad (5)$$

which consists of a volumetric part ψ^{vol} and an isochoric part $\bar{\psi}$. Throughout this manuscript, we analyze three different formulations for the isochoric part $\bar{\psi}$ while keeping the volumetric part identical. The additive decomposition of the free energy manifests itself in the Piola-Kirchhoff stress,

$$\boldsymbol{S}=2\frac{\partial\psi}{\partial\boldsymbol{C}}=\boldsymbol{S}^{\mathrm{vol}}+\boldsymbol{S}^{\mathrm{iso}}, \quad (6)$$

where the volumetric and isochoric parts take the following explicit representations,

$$\begin{aligned}\boldsymbol{S}^{\mathrm{vol}}&=2\frac{\partial\psi^{\mathrm{vol}}}{\partial\boldsymbol{C}}=J\,p\,\boldsymbol{C}^{-1}\\ \boldsymbol{S}^{\mathrm{iso}}&=2\frac{\partial\bar{\psi}}{\partial\boldsymbol{C}}=J^{-2/3}\mathbb{P}:\bar{\boldsymbol{S}}.\end{aligned} \quad (7)$$

The volumetric part depends primarily on the pressure $p=\partial\psi^{\mathrm{vol}}/\partial J$, which we have to prescribe constitutively in the context of incompressibility. The isochoric part depends on the second order tensor $\bar{\boldsymbol{S}}$, with

$$\bar{\boldsymbol{S}}=2\frac{\partial\bar{\psi}}{\partial\bar{\boldsymbol{C}}}=2\bar{\psi}_1\boldsymbol{I}+2\bar{\psi}_4\boldsymbol{N}, \quad (8)$$

where we have introduced the common abbreviation $\bar{\psi}_i=\partial\bar{\psi}/\partial\bar{I}_i$ for the scalar derivatives of the isochoric free energy function $\bar{\psi}$, which we will specify in detail in the sequel. The fourth order tensor $\mathbb{P}=\mathbb{I}-\frac{1}{3}\boldsymbol{C}^{-1}\otimes\boldsymbol{C}$ denotes the isochoric projection tensor in terms of the fourth order identity tensor $\mathbb{I}=\frac{1}{2}[\boldsymbol{I}\bar{\otimes}\boldsymbol{I}+\boldsymbol{I}\underline{\otimes}\boldsymbol{I}]$, with the understanding that $\{\bullet\bar{\otimes}\bigcirc\}_{ijkl}=\{\bullet\}_{ik}\{\bigcirc\}_{jl}$ and $\{\bullet\underline{\otimes}\bigcirc\}_{ijkl}=\{\bullet\}_{il}\{\bigcirc\}_{jk}$. To efficiently solve the nonlinear boundary value problem, we linearize the Piola-Kirchhoff stress $\boldsymbol{S}$ with respect to the right Cauchy-Green deformation tensor $\boldsymbol{C}$ to obtain the fourth order tangent moduli

$$\mathbb{C}=4\frac{\partial^2\psi}{\partial\boldsymbol{C}\otimes\partial\boldsymbol{C}}=2\frac{\partial\boldsymbol{S}}{\partial\boldsymbol{C}}=\mathbb{C}^{\mathrm{vol}}+\mathbb{C}^{\mathrm{iso}}, \quad (9)$$

which we can again decompose into volumetric and isochoric parts,

$$\begin{aligned}\mathbb{C}^{\mathrm{vol}}&=2\frac{\partial\boldsymbol{S}^{\mathrm{vol}}}{\partial\boldsymbol{C}}=J\,\tilde{p}\,\boldsymbol{C}^{-1}\otimes\boldsymbol{C}^{-1}-2J\,p\mathbb{I}_{\boldsymbol{C}^{-1}}\\ \mathbb{C}^{\mathrm{iso}}&=2\frac{\partial\boldsymbol{S}^{\mathrm{iso}}}{\partial\boldsymbol{C}}=J^{-4/3}\mathbb{P}:\bar{\mathbb{C}}:\mathbb{P}^{\mathrm{t}}+\tfrac{2}{3}[J^{-2/3}\bar{\boldsymbol{S}}:\boldsymbol{C}\,\bar{\mathbb{P}}-[\bar{\boldsymbol{S}}\otimes\boldsymbol{C}^{-1}]^{\mathrm{sym}}].\end{aligned} \quad (10)$$

The volumetric part is parameterized in terms of the pressure p, where we have introduced the abbreviation $\tilde{p}=p+J\,\partial p/\partial J$. The isochoric part depends on the fourth order tensor $\bar{\mathbb{C}}$, with

$$\bar{\mathbb{C}}=2\frac{\partial\bar{S}}{\partial\bar{\boldsymbol{C}}}=4[\bar{\psi}_{11}\boldsymbol{I}\otimes\boldsymbol{I}+2\bar{\psi}_{14}[\boldsymbol{I}\otimes\boldsymbol{N}]^{\mathrm{sym}}+\bar{\psi}_{44}\boldsymbol{N}\otimes\boldsymbol{N}], \quad (11)$$

with the common abbreviation $\bar{\psi}_{ij} = \partial^2\bar{\psi}/\partial\bar{I}_i\partial\bar{I}_j$ for the second derivatives. Here, $\bar{\mathbb{P}}=\mathbb{I}_{\mathrm{C}^{-1}} - \frac{1}{3}\boldsymbol{C}^{-1} \otimes \boldsymbol{C}^{-1}$ and $\mathbb{I}_{\mathrm{C}^{-1}}=\frac{1}{2}[\boldsymbol{C}^{-1} \bar{\otimes} \boldsymbol{C}^{-1}+\boldsymbol{C}^{-1} \underline{\otimes} \boldsymbol{C}^{-1}]$ are two additional fourth order tensors related to the isochoric projection. From the Piola-Kirchhoff stress $\boldsymbol{S}$ and the Lagrangian tangent moduli $\mathbb{C}$, we can calculate the Cauchy stress σ and the Eulerian tangent moduli $\mathbb{c}$through the corresponding push forward operations

$$\sigma=\frac{1}{J}\boldsymbol{F} \cdot \boldsymbol{S} \cdot \boldsymbol{F}^{\mathrm{t}} \text{ and } \mathbb{c}=\frac{1}{J}[\boldsymbol{F}\bar{\otimes}\boldsymbol{F}]:\mathbb{C}:[\boldsymbol{F}^{\mathrm{t}}\bar{\otimes}\boldsymbol{F}^{\mathrm{t}}].$$

3.2.1 Isotropic Model—The first model, the Neo-Hookean model, is the most simplistic constitutive model for nonlinear hyperelastic materials. Isotropic in nature, it neglects the characteristic anisotropic microstructure of mitral leaflet tissue. The isochoric part of its free energy $\bar{\psi}$ of Equation (5) is parameterized exclusively in terms of the first isochoric invariant $\bar{I}_1$ scaled by the single material parameter c_0,

$$\bar{\psi}=c_0[\bar{I}_1 - 3]. \quad (12)$$

In the limit of infinitesimal strains, the parameter c_0 corresponds to one half of the shear modulus μ. The isochoric part of the Piola-Kirchhoff stress $\bar{\boldsymbol{S}}$ of Equation (8) reduces a purely isotropic formulation according to the coefficients

$$\bar{\psi}_1=c_0 \quad \text{and} \quad \bar{\psi}_4=0. \quad (13)$$

The isochoric Neo-Hookean tangent moduli $\bar{\mathbb{C}}$ of Equation (11) vanish identically since

$$\bar{\psi}_{11}=0 \quad \text{and} \quad \bar{\psi}_{14}=0 \quad \text{and} \quad \bar{\psi}_{44}=0. \quad (14)$$

3.2.2 Coupled Anisotropic Model—The second model, the May-Newman model, is an anisotropic constitutive model introduced exclusively for mitral valve tissue, initially to characterize the homogeneous response during biaxial testing [34], and later to characterize the heterogeneous response of the entire mitral valve complex [40]. Outside the mitral valve community, it remains largely unknown, partly because its convexity properties have not been analyzed thoroughly to date. The May-Newman model introduces an inherent constitutive coupling between the isotropic and anisotropic material response. Transversely isotropic in nature, it is characterized through a single representative fiber family. Its isochoric free energy $\bar{\psi}$ of Equation (5) is parameterized in terms of the first and fourth isochoric invariants $\bar{I}_1$ and $\bar{I}_4$,

$$\bar{\psi}=c_0\,[\exp(c_1[\bar{I}_1 - 3]^2+c_2[\bar{I}_4 - 1]^2) - 1]. \quad (15)$$

The coefficients for the isochoric part of the Piola-Kirchhoff stress $\bar{\boldsymbol{S}}$ of Equation (8)

$$\begin{aligned}\bar{\psi}_1&=2\,c_0c_1[\bar{I}_1 - 3]\exp(c_1[\bar{I}_1 - 3]^2+c_2[\bar{I}_4 - 1]^2)\\ \bar{\psi}_4&=2\,c_0c_2[\bar{I}_4 - 1]\exp(c_1[\bar{I}_1 - 3]^2+c_2[\bar{I}_4 - 1]^2)\end{aligned} \quad (16)$$

and for the isochoric part of the tangent moduli $\bar{\mathbb{C}}$ of Equation (11)

$$\begin{aligned}\bar{\psi}_{11}&=2\,c_0c_1[\,1+2c_1[\bar{I}_1-3]^2]\exp(c_1[\bar{I}_1-3]^2+c_2[\bar{I}_4-1]^2)\\ \bar{\psi}_{14}&=4\,c_0c_1c_2[\bar{I}_1-3][\bar{I}_3-1]\exp(c_1[\bar{I}_1-3]^2+c_2[\bar{I}_4-1]^2)\\ \bar{\psi}_{44}&=2\,c_0c_2[\,1+2c_2[\bar{I}_3-1]^2]\exp(c_1[\bar{I}_1-3]^2+c_2[\bar{I}_4-1]^2)\end{aligned}\quad(17)$$

are exponential functions weighted by the three material parameters c_0, c_1, and c_2. The model assumes that its fibers can only bear load under tension, $\bar{I}_4 \geq 1$, not contributing to stress and stiffness under compressive loading, $\bar{I}_4 < 1$. Unlike most transversely isotropic models for non-living tissue, the May-Newman model is characterized through a constitutive coupling between the first and fourth invariants. This implies that its mixed second derivatives do not vanish identically, $\bar{\psi}_{14} \neq 0$.

3.2.3 Decoupled Anisotropic Model—The third model, the Holzapfel model, is an anisotropic constitutive model originally designed for arterial tissue [13]. While its convexity aspects have been thoroughly investigated, it has never been adopted to model the heterogeneous response of the mitral valve complex. The initial Holzapfel model is inherently modular with two decoupled terms, one for the isotropic and one for the anisotropic material response. Transversely isotropic in nature, it incorporates a single representative fiber family. Similar to the coupled model, its isochoric free energy $\bar{\psi}$ of Equation (5) is parameterized in terms of the first and fourth isochoric invariants $\bar{I}_1$ and $\bar{I}_4$,

$$\bar{\psi}=c_0\,[\bar{I}_1-3]+\frac{c_1}{2c_2}[\exp(c_2[\kappa\bar{I}_1+[\,1-3\kappa]\bar{I}_4-1]^2)-1]. \quad (18)$$

The coefficients for the isochoric part of the Piola-Kirchhoff stress $\boldsymbol{S}$ of Equation (8)

$$\begin{aligned}\bar{\psi}_1&=c_0+c_1\kappa\,[\kappa\bar{I}_1+[\,1-3\kappa]\bar{I}_4-1]\exp(c_2[\kappa\bar{I}_1+[\,1-3\kappa]\bar{I}_4-1]^2)\\ \bar{\psi}_4&=c_1[\,1-3\kappa][\kappa\bar{I}_1+[\,1-3\kappa]\bar{I}_4-1]\exp(c_2[\kappa\bar{I}_1+[\,1-3\kappa]\bar{I}_4-1]^2)\end{aligned}\quad(19)$$

and for the isochoric part of the tangent moduli $\mathbb{C}$ of Equation (11)

$$\begin{aligned}\bar{\psi}_{11}&=c_1\kappa^2 &&[\,1+2\,c_2[\kappa\bar{I}_1+[\,1-3\kappa]\bar{I}_4-1]]\exp(c_2[\kappa\bar{I}_1+[\,1-3\kappa]\bar{I}_4-1]^2)\\ \bar{\psi}_{14}&=c_1\kappa[\,1-3\kappa] &&[\,1+2\,c_2[\kappa\bar{I}_1+[\,1-3\kappa]\bar{I}_4-1]]\exp(c_2[\kappa\bar{I}_1+[\,1-3\kappa]\bar{I}_4-1]^2)\\ \bar{\psi}_{44}&=c_1[\,1-3\kappa]^2 &&[\,1+2\,c_2[\kappa\bar{I}_1+[\,1-3\kappa]\bar{I}_4-1]]\exp(c_2[\kappa\bar{I}_1+[\,1-3\kappa]\bar{I}_4-1]^2)\end{aligned}\quad(20)$$

are again exponential functions weighted by the three material parameters c_0, c_1, and c_2. For $c_1 = 0$ and $c_2 = 0$, we recover the original Neo-Hookean model. Similar to the May-Newman model, the fiber contributions act in tension only, $\bar{I}_4 \geq 1$, and are inactive under compressive loading, $\bar{I}_4 < 0$. In contrast to the original decoupled version of the Holzapfel model [18], this revised version accounts for a constitutive coupling of the first and fourth invariants through the additional parameter κ to incorporate microstructural fiber dispersion [13]. The lower limit of $\kappa = 0$ represents the initial decoupled model with no fiber dispersion, no constitutive coupling between the first and fourth invariants, and vanishing mixed second derivatives, $\bar{\psi}_{14} = 0$ [18]. The upper limit of $\kappa=\frac{1}{3}$ represents the random fiber dispersion of an isotropic material with vanishing anisotropic terms, $\bar{\psi}_4 = 0$, $\bar{\psi}_{14} = 0$, and $\bar{\psi}_{44} = 0$.

3.3 Finite Element Modeling

3.3.1 Finite Element Software—We performed all simulations with the commercially available, implicit finite element solver Abaqus Standard Version 6.9 using the general-

purpose, finite strain shell element S3R [1], which adopts discrete Kirchhoff thin shell kinematics [40].

3.3.2 Reference Configuration and Simulation Interval—Similarly to our previous inverse finite element study [21], we chose the image just before leaflet separation as the reference configuration and as the start point of our simulation, see Figure 4. In eight time steps, we performed finite element simulations from this reference point, in reverse direction, to end-systole. We selected this particular simulation interval throughout isovolumic relaxation, because the the mitral valve is closed, and hemodynamic effects are negligible. In addition, during isovolumic relaxation, the effects of possibly interfering contracting cells are minimized.

3.3.3 Boundary Conditions—Throughout the inverse finite element analysis, we applied inhomogeneous Dirichlet boundary conditions to all nodes on the boundary during the entire simulation interval, see Figure 8. We prescribed the positions for these boundary nodes using the nodal coordinates of the experimental subdivision meshes at the respective time points. In other words, throughout the entire simulation, we prescribed the nodal positions of the annular and free edges using the experimentally acquired boundary marker coordinates, while we calculated the positions of all internal nodes for varying sets of material parameters [21].

3.3.4 External Loading—The primary load on the mitral leaflet within the simulation interval is the transvalvular pressure, i.e., the pressure difference between the left ventricle and the left atrium. We determined the average pressure difference for all animals from hemodynamic measurements for each time-aligned data point, see Figure 4, and applied it to the ventricular surface of the discretized mitral valve geometry, see Figure 8.

3.3.5 Chordae Tendineae—The chordae tendineae attach to the free edge, the leaflet center, and the region close to the annulus, see Figure 1. Since we prescribe the nodal positions of the free edge and of the annulus as Dirichlet boundary conditions, see Section 3.3.3, the effects of the chordae tendineae at the free edge and at the annulus are inherently built into the model. However, we have to account for the chordae tendineae in the belly region. Here, we modeled the chordae tendineae as tension only rods inserting into the leaflet center [41]. We modeled the chordae material as incompressible Neo-Hookean according to Equation (12) and assumed a total cross-sectional area of 1mm^2 for each branch.

3.3.6 Prestrain—To explore the effect of prestrain on the parameter identification of both anisotropic hyperelastic models, we prestrained the leaflet with an isotropic in-plane Green-Lagrange area strain

$$\boldsymbol{E}^{\text{pre}}=\frac{1}{2}\left[\boldsymbol{F}^{\text{pret}}\cdot\boldsymbol{F}^{\text{pre}}-\boldsymbol{I}\right]=E^{\text{pre}}\,\boldsymbol{I},$$

prescribing prestrain levels E^{pre} of 0%, 30%, and 60% following prestrain protocols developed in our group [12,48]. We calculated the corresponding prestretch $\lambda^{\text{pre}} = [2\,E^{\text{pre}} + 1]^{1/2}$ of 1.00, 1.27, and 1.48 such that $\boldsymbol{F}^{\text{pre}} = \lambda^{\text{pre}}\,\boldsymbol{I}$. Subsequently, we shrunk the leaflet geometry by scaling the nodal coordinates of the reference configuration with the reciprocal stretch values $1/\lambda^{\text{pre}}$ of 1.00, 0.79, and 0.67. In a preconditioning step, we displaced each node of the shrunk leaflet geometry to its original position creating an isotropic Green-Lagrange area prestrain of 0%, 30%, and 60% across the entire anterior leaflet. After

verifying the prescribed prestrain levels, we applied the external pressure loading according to Section 3.3.4.

3.4 Parameter Identification

3.4.1 Sensitivity Analysis—To study and demonstrate the effect of varying input parameters on the parameter identification, we performed a series of sensitivity analyses. For the sake of simplicity, we used the isotropic Neo-Hookean model for these studies. Its conceptual simplicity significantly decreased both simulation time and optimization effort. We selected a set of relevant input parameters and varied the Neo-Hookean parameter c_0 from 0.1MPa to 100MPa in steps of 0.1MPa. Starting from the reference configuration, for each value of c_0, we performed a finite element analysis for all eight time steps. As a representative error measure, we calculated the average nodal displacement error e as the distance between all $m = 1, .., n_m$ experimentally measured inner leaflet markers $\varphi_{t,m}^{exp}$ and all computationally simulated inner leaflet markers $\varphi_{t,m}^{sim}$, and summed it over all $t = 0, .., n_t$ time steps

$$e=\frac{1}{n_t}\frac{1}{n_m}\sum_{t=0}^{n_t}\sum_{m=1}^{n_m}\|\boldsymbol{\varphi}_{t,m}^{exp}-\boldsymbol{\varphi}_{t,m}^{sim}\|.$$

In our case, the number of inner leaflet markers was $n_m = 9$ and the number of times steps was $n_t = 8$. For each input parameter we identified the value for the Neo-Hooke parameter c_0 that minimized this average nodal displacement error e.

First, to quantify the sensitivity of the model with respect to leaflet thickness, we varied the thickness of the linear triangular shell elements between 0.5mm and 4.0mm in intervals of 0.5mm and determined its impact on the optimal parameter c_0.

Second, since the exact locations of the chordal insertion sites are unknown, we chose three alternative chordae locations and investigated the model's sensitivity to changes in insertion site. In particular, we inserted chordae close to the annulus toward the anterior and posterior commissures, see Figure 9A, close to the annulus toward the midline of the anterior leaflet, see Figure 9B, and closer to the free edge, see Figure 9C, and connected them to the papillary muscle tips. In addition, to determine the sensitivity of the model to the number of chordae, we compared the simulation with seven chordae to the simulation with one chord, see Figures 9C and 9D. For the sake of comparison, we kept the the total cross-sectional area of each branch of chordae constant at $1mm^2$.

Third, to quantify the sensitivity of the model with respect to chordae stiffness, we varied the Neo-Hookean stiffness c_0 of the chordae between 5MPa and 40MPa in intervals of 5MPa.

Fourth, we systematically varied the transverse shear stiffness, a structural parameter inherent to the finite element formulation for the selected shell element. Since this parameter is a structural parameter with no clear physical interpretation, we investigated different shear stiffness values of 10MPa, 100MPa, and 1000MPa and quantified the corresponding optimal Neo-Hookean parameter c_0.

3.4.2 Parameter Identification—To identify the material parameters of the different constitutive models, we performed an inverse finite element analysis, similar to the procedure described in Section 3.4.1. However, now, we apply a genetic algorithm using MATLAB, to systematically minimize the average nodal displacement error e by varying all

material parameters simultaneously. Starting with an initial parameter set, we performed a first generation of finite element simulations. After the simulation for each parameter set, we compared the experimentally measured marker positions $\varphi_{t,m}^{\exp}$ of the $m = 1, .., n_m$ inner nodes for each $t = 0, .., n_t$ time step with the computationally simulated marker positions $\varphi_{t,m}^{\mathrm{sim}}$ to calculate the average nodal displacement error e. Again, the number of inner markers was $n_m = 9$ and the number of time steps was $n_t = 8$. Whenever the simulation did not converge, we assigned an error value that was larger than previously encountered values for converged solutions. Based on the average nodal displacement error e, the genetic algorithm generated a new input parameter set through 20% mutation and 80% cross-over. The genetic algorithm iteratively minimized the error until it reached a user-defined convergence criterion of of 10^{-6}. For visualization purposes, we calculated the nodal displacement error at the last simulation time step $t = 8$, and analyzed its distribution across the leaflet using color contour plots. After finding a converged parameter set, we repeated the optimization algorithm for varying population sizes and initial parameters to ensure that the converged solution represented a global minimum. Figure 10 illustrates the genetic algorithm in a representative flow chart.

For the parameter identification, we chose the finite element discretization with 1920 elements and 1017 nodes, see Figure 5, a leaflet thickness of 1mm, a chordae insertion location closer to the free edge of the anterior leaflet, see Figure 9C, a chordae stiffness of 20MPa, and a transverse shear stiffness of 100MPa. In addition, to investigate the impact of prestrain on the material parameters, we performed the three optimization runs with 0%, 30%, and 60% prestrain.

4 Results

4.1 Sensitivity Analysis for Isotropic Model

Figure 11 summarizes the results of the sensitivity study of the isotropic Neo-Hookean model with respect to mesh refinement, element thickness, and chordae stiffness. Figure 11A illustrates the results of the mesh refinement study. Mesh refinement displays satisfying convergence at the third subdivision level with 1920 elements. Accordingly, we selected the discretization with 1920 elements and 1017 nodes for all subsequent simulations. Figures 11B illustrates the sensitivity with respect to leaflet thickness. For varying leaflet thicknesses, the optimal stiffness parameter decreased super-linearly from 76.8MPa at a thickness of 0.5mm to 6.3MPa at a thickness of 4mm. Figures 11C shows the sensitivity with respect to chordal stiffness. For varying chordae stiffnesses, the optimal stiffness parameter decreased almost linearly from 82.8MPa at a chordae stiffness of 5MPa to 48.5MPa at a chordae stiffness of 40MPa. For varying number of chordae at the same overall stiffness, the optimal stiffness parameter remained virtually unaffected, varying only marginally from 63.7MPa for seven chordae to 65.4MPa for one chord. Figure 9 displays the different chordal locations considered in this study. For varying chordal locations, the optimal stiffness parameter varied only marginally between 77.5MPa for location A, 85.0MPa for location B, and 63.7MPa for location C. For varying transverse shear stiffnesses, the optimal stiffness parameter displayed strong variations. A transverse shear stiffness of 10MPa yielded an optimal stiffness parameter c_0 of 23.2MPa, 100MPa yielded 63.7MPa, and 1000MPa yielded 173.7MPa. Overall, the sensitivity analysis revealed that the stiffness parameter c_0 for the Neo-Hookean model was sensitive to element thickness, chordae location, chordae stiffness, and transverse shear stiffness.

Figure 12 shows a representative displacement error distribution of the isotropic Neo-Hookean model. Qualitatively, all error plots for the Neo-Hookean model showed similar contour patterns. Throughout the entire leaflet, maximum nodal displacement errors were in

the submillimeter range. In the belly region, nodal error values were negative, implying that the experimental leaflet, based on the original marker coordinates, moved farther into the atrium than the simulated leaflet. In the annular region, nodal error values were positive, implying that the experimental leaflet, based on the original marker coordinates, moved less far into the atrium than the simulated leaflet. On the annular and free edge boundaries, where nodal positions were prescribed in terms of Dirichlet boundary conditions, nodal errors were zero.

Figure 13 displays the regional variation of the leaflet thickness when optimized for the isotropic model. The regional variation of the displacement error in Figure 12 motivated a follow-up parameter identification, in which we assigned each of the 1920 finite elements its individual leaflet thickness. We identified these 1920 thickness parameters using an inverse finite element analysis according to the flow chart of Figure 10 with the overall goal to minimize the total displacement error. Figure 13 displays the resulting thickness distribution with a maximum leaflet thickness of 3.0mm close to the annulus and a minimum leaflet thickness of 0.1mm around the leaflet belly and close to the free edge.

Figure 14 displays the regional variation of the bending stiffness when optimized for the isotropic model. Although we performed a fully nonlinear parameter identification, here, we display the intuitive linearized bending stiffness EI, where E is the equivalent to Young's modulus in the linear regime and I is the moment of inertia, which scales with the thickness to the power of three. The bending stiffness is a structural parameter, which inherently combines information about leaflet stiffness and thickness. Accordingly, its distribution agreed qualitatively with the thickness distribution in Figure 13, but displays larger overall variations. We observed a maximum bending stiffness of 50Nmm^2 close to the annulus and a minimum bending stiffness of 0.05Nmm^2 around the leaflet belly and close to the free edge.

4.2 Parameter Identification for Anisotropic Models

Figure 15 shows that for both anisotropic models, coupled and decoupled, the optimization procedure yielded qualitatively similar displacement error contours as for the isotropic model. Errors were again in the submillimeter range, with a qualitatively similar pattern independent of the level of prestrain. Again, while in the belly region nodal errors were predominantly negative, nodal error in the annular region were predominantly positive.

Table 1 summarizes the average nodal displacement error for the coupled and the decoupled anisotropic models for all three levels of prestrain. Quantitatively, increasing degree of prestrain increased the error. Independent of the degree of prestrain, average nodal displacement errors were consistently smaller for the decoupled model than for the coupled model. These trends are in agreement with the nodal error distributions displayed in Figure 15.

Table 2 summarizes the results from the parameter identification for the coupled and decoupled anisotropic models for all three prestrain levels. Unfortunately, the stiffness parameters c_0, c_1, and c_2 take different interpretations in both models, some even with different units, and we cannot directly compare their values. The decoupled anisotropic model parameter c_0, however, corresponds directly to the isotropic parameter c_0, and lies within the range of the values reported in Figure 11.

To visualize the constitutive behavior of the calibrated coupled and decoupled models, we performed virtual homogeneous uniaxial tensile tests in the circumferential and radial directions mimicking the ex vivo response in terms of the identified material parameter values summarized in Table 2. Figure 16 illustrates the sensitivity of the constitutive

response with respect to the prestrain level. To fit the same behavior of the mitral leaflet in vivo, the parameter identification at 0% prestrain yields a much stiffer ex vivo response, indicated through the dotted lines, than the parameter identification at 30% prestrain, dashed lines, and at 60% prestrain, dash-dotted lines. Overall, by increasing the in vivo prestrain level, we obtain parameter sets, which predict a much softer ex vivo response, resulting in lower Cauchy stresses at the same stretch level.

Figures 16A and 16B show the nominal or Cauchy stress plotted over uniaxial stretch using the calibrated coupled anisotropic model at the three different prestrain levels. In both radial and circumferential directions the model clearly displays the characteristic nonlinear, strain-stiffening response of collagenous soft tissues. Figures 16C and 16D illustrate the stress-stretch behavior, now using the calibrated decoupled anisotropic model at the three different prestrain levels. In the circumferential direction, the decoupled model predicts a similar strain-stiffening response as the coupled model. In the radial direction, however, the decoupled model behaves almost linearly and fails to reproduce the characteristic stress locking.

Figure 16 compares the predicted uniaxial stress-stretch behavior for both models to the uniaxial stress-stretch behavior of the May-Newman model fit to ex vivo biaxial test data indicated by the solid lines [34]. The experiment displays a strong nonlinear stress-stretch behavior in both circumferential and radial directions. In circumferential direction, both anisotropic models fit the ex vivo data based stress-stretch response best for 30% prestrain, Figures 16A and 16C. In radial direction, the coupled model fits the data best for 30% prestrain, Figure 16B, while the decoupled model, due to its lack of nonlinearity, shows a poor fit, independent of the prestrain level, Figure 16D.

Figure 17 compares the maximum principal Green-Lagrange strains between end-isometric relaxation and end-systole. The left and right columns display the strains for the coupled and decoupled models, respectively, both evaluated at three levels of prestrain. Qualitatively, strain contours vary little between the two anisotropic models at any of the prestrain levels. Strains are largest toward the free edge and in the belly of the anterior leaflet and smallest toward the annular regions. Quantitatively, within each level of prestrain, strain plots were conceptually similar between the two anisotropic models. Figure 17 demonstrates the multiplicative effect of prestrain on leaflet strain. While maximum principal strains for 0% prestrain reached peak values of approximately 10% percent, maximum principal strains for 30% and 60% prestrain reached peak values of approximately 70% and 100%, respectively.

5 Discussion

In this study we have, for the first time, identified the material parameter values of three prominent nonlinear hyperelastic constitutive models for mitral leaflet tissue from in vivo data. In particular, we have calibrated the coupled May Newman model originally introduced for mitral valve tissue under homogeneous biaxial loading [34], and later for the heterogeneous response of the entire mitral valve complex [40]. In addition, we have calibrated the decoupled Holzapfel model that has become widely known for anisotropic soft tissues such as arteries [18], here enhanced to incorporate fiber dispersion [13]. To put our study into perspective, we have performed systematic sensitivity analyses of important structural parameters using an isotropic Neo-Hookean model. Most remarkably, the constitutive response was found to be highly sensitive to the level of prestrain.

5.1 Sensitivity Analysis

Before discussing the results of the parameter identification, it is important, at this point, to reflect on the results of the sensitivity study. We observed that the finite element simulation

was highly sensitive to model parameters such as leaflet thickness, chordae stiffness, and transverse shear stiffness. Sensitivity to leaflet thickness originates from the thickness dependence of both tensile stiffness and bending stiffness. While the tensile stiffness increases linearly with leaflet thickness, the bending stiffness increases with the leaflet thickness to the power of three. The latter may explain the nonlinear relationship between the optimal stiffness parameter and the leaflet thickness as documented in Figure 11B.

Here, we have assumed a homogeneous thickness distribution across the entire mitral leaflet. The error patterns in Figures 12 and 15 are, at least in part, caused by this homogeneous thickness assumption [41]. To minimize this error, we performed a parameter identification, in which we assigned each element its individual thickness, and identified these thicknesses using an inverse finite element analysis. The calculated thickness and bending stiffness distributions in Figures 13 and 14 are in excellent agreement with recent anatomic studies, which reported that the leaflet is the thickest close to the annulus and the thinnest close to the free edge, decreasing gradually from central belly to free edge [19]. A uniform thickness overestimates the leaflet stiffness in the belly region and close to the free edge, while it underestimates the stiffness close to the annulus [22]. In turn, overestimating leaflet thickness results in smaller leaflet deflections into the atrium than measured experimentally, while underestimating leaflet thickness close to the annulus results in larger deflections of the leaflet into the atrium. The former generates a negative error, displayed in blue, while the latter generates a positive error, displayed in red, see Figures 12 and 15.

The sensitivity of the optimal stiffness parameter with respect to chordae stiffness may follow from increased chordae forces counteracting the transvalvular pressure that displaces the mitral leaflet into the atrium. As this reaction force increases, the stiffness of the leaflet itself decreases to minimize the displacement error between experiment and simulation as documented in Figure 11C.

Lastly, we observed that with increasing values of transverse shear stiffness, leaflet buckling occurred at higher stiffness parameters. As leaflet buckling significantly increased the displacement error, the transverse shear stiffness presented an upper limit for the optimal stiffness parameter. This explains the observed sensitivity of the optimal stiffness parameter to changes in transverse shear stiffness as documented in Figure 11D.

In contrast to leaflet thickness, chordae stiffness, and transverse shear stiffness, neither chordae insertion location nor number of chords affected the optimal stiffness parameter to a significant extent.

In conclusion, when interpreting the results of this study, it is important to be aware of the sensitivity of the computational model with respect to various input parameters and, ideally, to quantify their impact on the final end result. While most input parameters have a clear physical interpretation, e.g., leaflet thickness or chordae stiffness, other parameters have never been reported, e.g., transverse shear stiffness. As finite element modeling of the mitral valve is gaining increased importance, from both a scientific and a clinical perspective, it might be worthwhile to determine values such as the transverse shear stiffness experimentally for future work.

5.2 Constitutive Modeling

We have investigated two commonly used anisotropic, hyperelastic constitutive models for mitral valve tissue, the coupled May-Newman model [34] and the decoupled Holzapfel model [18]. Both constitutive formulations are derived from a free energy function, which features an exponential term to capture the nonlinear tensile stiffening of soft collagenous tissues. Both free energy functions capture the isotropic behavior of the ground substance

through the first deviatoric invariant $\bar{I}_1$, i.e., the trace of the deviatoric deformation, and the anisotropic behavior of the collagenous microstructure through the fourth deviatoric invariant $\bar{I}_4$, i.e., the square of the fiber stretch. The ground substance behaves exponentially in the coupled model and linearly in the original decoupled model. While isotropic and anisotropic terms are coupled multiplicatively in the coupled May-Newman model [34], they are coupled additively in the original decoupled Holzapfel model [18]. To address this deficiency, the modified Holzapfel model introduces an additional microstructural parameter κ, which takes into account fiber dispersion around a preferred direction [13]. A κ value of zero results in no dispersion, while a value of one third describes random dispersion characteristic for an isotropic material.

These distinct features in the free energy function strongly determine their appropriateness for modeling mitral valve tissue. Independent of the prestrain level, the average nodal displacement error was smaller for the decoupled model than for the coupled model. Hence, we might claim that the calibrated decoupled model displays a higher potential to capture the true in vivo behavior of mitral leaflet tissue. However, it is important to keep in mind that the dispersion-enhanced decoupled model, as implemented in this study, features an additional parameter κ, which allows us to greatly vary the character of the model from entirely isotropic to anisotropic. The coupled model features only the three stiffness parameters c_0, c_1, and c_2. The better performance of the decoupled model over the coupled model might therefore simply be a result of its larger number of parameters.

To characterize model performance, in addition to average nodal and regional displacement errors, we compared the mechanical behavior of both models to the original May-Newman model with parameters fit from biaxial ex vivo data [34]. The comparison clearly demonstrated the difference between the coupled model with an exponential isotropic ground substance and the decoupled model with a linear isotropic ground substance. While both models capture the exponential constitutive response in the circumferential fiber direction, the decoupled model fails to capture the exponential response in the radial cross-fiber direction.

In conclusion, both models show great promise to minimize the error between experiment and simulation. While the decoupled model minimizes the displacement error relative to the in vivo experiment to a larger extent, the coupled model captures the qualitative mechanical behavior observed in ex vivo experiments more appropriately.

5.3 Parameter Identification

In previous studies, our group has identified mitral leaflet parameters for an anisotropic linear elastic constitutive model [21,22]. In the current study, we have extended this work to two commonly used anisotropic nonlinear hyperelastic constitutive models. This step is particularly crucial as models of the mitral valve are becoming more commonly used, not only for basic science studies but also to understand human disease and to predict medical device performance. Since mitral valve tissue, under disease conditions and upon device implantation, may undergo large deformations [44,53], it is important to select the constitutive model appropriately. Hyperelastic constitutive models have become the models of choice for soft biological tissue in general, and mitral valve tissue in particular. Here, for the first time, we have identified material parameters for two such models, a coupled model and a decoupled model, based on in vivo data. Recent studies have reported a large discrepancy between the mitral leaflet stiffness measured in vivo and ex vivo [21]. This stiffness difference has motivated the hypothesis of active leaflet contraction [19], which was supported experimentally by a 40% to 58% stiffness increase in isovolumetric contraction compared to isovolumetric relaxation [22]. Systematic tissue histology in human tissue samples has confirmed the existence of active contractile smooth muscle cells in the

mitral valve leaflets [36,55]. Active contraction alone, however, does not seem capable of explaining a stiffness discrepancy of several orders of magnitude. Future studies with hyperelastic constitutive models will be necessary to compare the parameter values calibrated ex vivo to the parameters values calibrated in vivo as illustrated here. Beyond that, it is important to remember that the models calibrated here are based on sheep rather than on human data. It is therefore vital to be careful when extrapolating models based on our material parameter values to the human mitral valve.

5.4 Effect of Prestrain

An exciting recent study revealed that the anterior mitral leaflet is subject to considerable prestrain throughout the entire cardiac cycle [2]. To explore the effect of prestrain on the set of optimal material parameter values, we identified sets of material parameters for three different levels of prestrain, 0%, 30% and 60%. We found that material parameters were highly sensitive to the level of prestrain, with some parameter values varying up to four orders of magnitude. We believe that this effect is due to a prestrain-dependent shift of the linear regime, beyond which the stress-strain response experiences the characteristic stress locking. When starting from a prestrain level of 0% and superimposing the physiological strain amplitudes throughout the cardiac cycle of about 10% [44], we are operating in the linear regime of the stress-strain curve throughout the entire cardiac cycle [23]. As we increase the prestrain level, this operating point moves along the nonlinear stress-strain curve, beyond the linear regime, into the exponential stiffening region of the curve. At 0% prestrain, the optimization algorithm forces the linear region of the nonlinear stress-strain curve to be stiff enough, so that the anterior mitral leaflet sustains the transvalular pressure to minimize the error between the experiment and simulation. As we increase the prestrain level, the optimization algorithm enforces the same stiffness to the exponential stiffening region beyond the linear regime, creating an overall softer response than before. We can therefore interpret the physiological in vivo stiffness of the mitral leaflet as a function of both, the material parameters and the prestrain-defined point of operation.

Studies based on ex vivo experiments have reported cardiac cycle stretches of up to 1.7 [17,51], while in vivo experiments suggest stretch values that are considerably lower [44]. In addition, previous studies in our group have reported the in vivo anterior mitral leaflet stiffness to be orders of magnitude higher than found ex vivo [21,22]. Interestingly, at a prestrain level of 30%, the uniaxial stress-stretch curves of the coupled model and the decoupled model were able to match both, in vivo and ex vivo data. This motivates the hypothesis that prestrain of the order of 30% may, at least in part, explain the observed discrepancy between in vivo and ex vivo mechanics of the anterior mitral leaflet and the entire mitral valve complex.

Unfortunately, an exact quantification of prestrain levels in the mitral valve is currently only available for the mitral leaflet center [2]. For the lack of better data, we therefore assumed the prestrain to be volumetric and homogeneous across the entire leaflet. This simplification may explain the increasing displacement error, which we observed with increasing levels of prestrain. Future studies remain to be performed to confirm the first reported prestrain studies [2], and to accurately quantify prestrain across the entire anterior and posterior mitral leaflets.

As our study demonstrates, the incorporation of prestrain is crucial since prestrain does not simply affect leaflet strains in an additive manner; rather, it affects leaflet strains in a multiplicative sense. This multiplicative effect is illustrated in Figure 17. While at 0% prestrain, the leaflet strains remain between 0% and 10%, at 30% and 60% prestrain, the leaflet strains exceed 40% and 70% strain by far. By ignoring prestrain, we hugely

underestimate physiological strains and, consequently, stresses in biological tissues in general, and in mitral valve tissue in particular.

5.5 Limitations

This manuscript presents, for the first time, a nonlinear material parameter identification for mitral valve leaflet tissue based on in vivo data. Despite promising first results, this approach presents a number of limitations, which we have to keep in mind when interpreting our findings. First, the creation of smooth leaflet surfaces from discrete marker points induces an approximation error. We have previously shown that this error lies within the range of the experimental measurement error and we have discussed potential limitations when first introducing this approximation technique [14]. Ever since, we have successfully employed this technology, while continuously monitoring the range of the approximation error [3,4,29,44–47]. Second, histological studies have shown that in reality, the mitral leaflet varies in thickness, tapering from approximately 1.2mm at the annulus to 0.2mm at the free edge [19]. Rather than smoothly varying the leaflet thickness, we have chosen a uniform leaflet thickness thickness of 1.0mm here, to make our findings easily reproducible for others interested in simulating the mitral valve complex. As Figure 13 suggests, a revised model should include regionally varying leaflet thicknesses with a maximum leaflet thickness of 3.0mm close to the annulus and a minimum leaflet thickness of 0.1mm around the leaflet belly and close to the free edge [19,21]. This would help to further reduce the displacement error in Figure 12. Third, along the same lines, in reality, leaflet tissue possesses a highly inhomogeneous, layered microstructure [36], with material parameters varying across the leaflet [22] and throughout the cardiac cycle [19,55]. As Figure 11B shows, the leaflet stiffness is inversely correlated to its thickness, and these two parameters should not be studied in isolation. In Figure 14, we have optimized the leaflet stiffness and leaflet thickness for the isotropic model using a single structural parameter, the leaflet bending stiffness. We have shown that the optimal leaflet bending stiffness displays large regional variations. In our anisotropic parameter identification, however, we have assumed both stiffness and thickness to be homogeneous. In the near future, we plan to perform more sophisticated studies to investigate their regional and transmembrane variations using layered shell elements [42]. Fourth, we have not explicitly determined chordae stiffnesses and chordae locations. However, we have motivated our parameters from the linear sensitivity analysis in Section 3.4.1. Based on these results, we selected a chordae insertion site close to the free edge, see Figure 9C, and a chordae stiffness of 20MPa. Both are in good agreement with the corresponding literature [21]. Fifth, for simplicity, we have applied a prestrain of in-plane isotropic nature. However, experimental studies suggest that leaflet prestrain is actually anisotropic [2]. While this simplification has allowed us to identify general trends, anisotropic studies will be necessary to truly confirm and quantify the existence of prestrain in vivo. Last, and most importantly, an inverse finite element analysis is inherently limited by the available data set itself. Here, the mechanical loading state during isovolumic relaxation is primarily equibiaxial. Therefore, it is highly likely that the different modes of the structure are not stimulated equally, which may leave the identification process underdetermined. This might be a first ad hoc explanation, why the coupled model, characterized through three distinct material parameters, yields a more intuitive parameter identification than the uncoupled model characterized through four distinct parameters. Further studies will be necessary to investigate why the identified parameter values for the coupled anisotropic model converge nicely, while the parameters for the decoupled anisotropic model do not, see Table 2.

6 Conclusion

In this study we have, for the first time, identified the material parameter values for two commonly used anisotropic hyperelastic constitutive models for the mitral valve from in vivo data. Both models provide an excellent fit to the in vivo data, with local displacement errors in the sub-millimeter range. The decoupled Holzapfel model, originally designed for arterial tissue, provided a slightly better in vivo fit, indicated through a smaller average nodal displacement error. The coupled May-Newman model, originally designed for mitral valve tissue, provided a significantly better ex vivo fit, accurately capturing both circumferential and radial strain stiffening. For both models, the parameter identification was highly sensitive to the level of prestrain, with some parameter values varying up to four orders of magnitude. For example, for the coupled anisotropic model, the stiffness varied from 119,021kPa at 0% prestrain to 36kPa at 30% prestrain to 9kPa at 60% prestrain. Our findings motivate the hypothesis that prestrain, at least in part, may explain the observed discrepancy between ex vivo and in vivo measured mitral leaflet stiffnesses. Taking all our observations together, we recommend using the coupled anisotropic model with prestrains of 30%, a stiffness of $c_0 = 35.9$kPa, and weighting factors of $c_1 = 2.3$ and $c_2 = 9.8$, which modeled the in vivo behavior accurately and approximated the ex vivo characteristics most closely. In conclusion, we believe that our study provides valuable guidelines for modeling mitral valve mechanics, selecting appropriate constitutive models, and choosing physiologically meaningful parameter values. For future investigations, we highly recommend to incorporate the effect of prestrain, both experimentally and computationally, to verify the existence of prestrain, to quantify its magnitude, and to clarify its role in mitral valve mechanics.

Acknowledgments

The authors thank Neil B. Ingels for designing the experimental study; John-Peder Escobar Kvitting and Julia C. Swanson for performing the surgical procedures; Paul Chang, Eleazar P. Briones, Lauren R. Davis, and Kathy N. Vo for assisting during the surgery; Maggie Brophy and Sigurd Hartnett for digitizing marker images; and George T. Daughters III for computing four-dimensional marker coordinates data biplane two-dimensional images. This study was supported by the Stanford University BioX Fellowship to Manuel Rausch, by the Deutsche Herzstiftung Research Grant S/06/07 to Wolfgang Bothe, by the US National Institutes of Health grants R01 HL29589 and R01 HL67025 to D. Craig Miller, and by the US National Science Foundation CAREER award CMMI 0952021 and INSPIRE grant 1233054 to Ellen Kuhl.

References

1. Abaqus 6.9. Analysis User's Manual. SIMULIA. Dassault Systèmes. 2009.
2. Amini R, Eckert CE, Koomalsingh K, McGarvey J, Minakawa M, Gorman JH, Gorman RC, Sacks MS. On the in vivo deformation of the mitral valve anterior leaflet: Effects of annular geometry and referential configuration. Annals of Biomedical Engineering. 2012; 40:1455–1467. [PubMed: 22327292]
3. Bothe W, Kuhl E, Kvitting JP, Rausch MK, Göktepe S, Swanson JC, Farahmandnia S, Ingels NB, Miller DC. Rigid, complete annuloplasty rings increase anterior mitral valve leaflet strains in the normal beating ovine heart. Circulation. 2011; 124:S81–S96. [PubMed: 21911823]
4. Bothe W, Rausch MK, Kvitting JP, Echtner DK, Walther M, Ingels NB, Kuhl E, Miller DC. How do annuloplasty rings affect mitral annular strains in the normal beating ovine heart? Circulation. 2012; 126:S231–S238. [PubMed: 22965988]
5. Libby, P.; Bonow, RO.; Man, DL.; Zipes, DP. Braunwald's Heart Disease. A Textbook of Cardiovascular Medicine. Philadelphia: Saunders Elsevier; 2008.
6. Dal-Bianco JP, Aikawa E, Bischoff J, Guerrero JL, Handschumacher MD, Sullivan S, Johnson B, Titus JS, Iwamoto Y, Wylie-Sears J, Levine RA, Carpentier A. Active adaptation of the tethered mitral valve: insights into a compensatory mechanism for functional mitral regurgitation. Circulation. 2009; 120:334–342. [PubMed: 19597052]

7. Chaput M, Handschumacher MD, Guerrero JL, Holmvang G, Dal-Bianco JP, Sullivan S, Vlahakes GJ, Hung J, Levine RA. Leducq Foundation MITRAL Transatlantic Network Mitral leaflet adaptation to ventricular remodeling: prospective changes in a model of ischemic mitral regurgitation. Circulation. 2009; 120:S99–S103. [PubMed: 19752393]
8. Carpentier, A.; Adams, DH.; Filsoufi, F. Carpentier's Reconstructive Valve Surgery. From Valve Analysis to Valve Reconstruction. Missouri: Saunders Elsevier; 2010.
9. Cochran RP, Kunzelman KS, Chuong CJ, Sacks MS, Eberhart RC. Nondestructive analysis of mitral valve collagen fiber orientation. American Society of Artificial Organs Transactions. 1991; 37:M447–M448.
10. Einstein DR, Reinhall P, Nicosia M, Cochran RP, Kunzelman K. Dynamic finite element implementation of nonlinear, anisotropic hyperelastic biological membranes. Computer Methods in Biomechanics and Biomedical Engineering. 2003; 6:33–44. [PubMed: 12623436]
11. Einstein DR, Kunzelman KS, Reinhall PG, Cochran RP, Nicosia MA. Haemodynamic determinants of the mitral valve closure sound: a finite element study. Medical & Biological Engineering & Computing. 2004; 42:832–846. [PubMed: 15587476]
12. Famaey N, Vander Sloten J, Kuhl E. A three-constituent damage model for arterial clamping in computer-assisted surgery. Biomechanics and Modeling in Mechanobiology.
13. Gasser TC, Ogden RW, Holzapfel GA. Hyperelastic modelling of arterial layers with distributed collagen fibre orientations. Journal of the Royal Society Interface. 2006; 3:15–35.
14. Göktepe S, Bothe W, Kvitting JP, Swanson J, Ingels NB, Miller DC, Kuhl E. Anterior mitral leaflet curvature in the beating ovine heart. A case study using videofluoroscopic markers and subdivision surfaces. Biomechanics and Modeling in Mechanobiology. 2010; 9:281–293. [PubMed: 19890668]
15. Grashow JS, Yoganathan AP, Sacks MS. Biaxial stress-stretch behavior of the mitral valve anterior leaflet at physiological strain rates. Annals of Biomedical Engineering. 2006; 34:315–325. [PubMed: 16450193]
16. Grashow JS, Sacks MS, Liao J, Yoganathan AP. Planar biaxial creep and stress relaxation of the mitral valve anterior leaflet. Annals of Biomedical Engineering. 2006; 34:1509–1518. [PubMed: 17016761]
17. He Z, Ritchie J, Grashow JS, Sacks MS, Yoganathan AP. In vitro dynamic strain behavior of the mitral valve posterior leaflet. Journal of Biomechanical Engineering. 2005; 127:504–511. [PubMed: 16060357]
18. Holzapfel GA, Gasser TC, Ogden RW. A new constitutive framework for anterial wall mechanics and a comparative study of material models. Journal of Elasticity. 2000; 61:1–48.
19. Itoh A, Krishnamurthy G, Swanson J, Ennis D, Bothe W, Kuhl E, Karlsson M, Davis L, Miller DC, Ingels NB. Active stiffening of mitral valve leaflets in the beating heart. American Journal of Physiology - Heart and Circulatory Physiology. 2009; 296:H1766–H1773. [PubMed: 19363135]
20. Jassar AS, Brinster CJ, Vergnat M, Robb D, Eperjesi TJ, Pouch AM, Cheung AT, Weiss SJ, Acker MA, Gorman JH, Gorman RC, Jackson BM. Quantitative mitral valve modeling using real-time three-dimensional echocardiography: Technique and repeatability. Annals of Thoracic Surgery. 2011; 91:165–171. [PubMed: 21172507]
21. Krishnamurthy G, Ennis DB, Itoh A, Bothe W, Swanson JC, Karlsson M, Kuhl E, Miller DC, Ingels NB. Material properties of the ovine mitral valve anterior leaflet in vivo from inverse finite element analysis. American Journal of Physiology - Heart and Circulatory Physiology. 2008; 295:H1141–H1149. [PubMed: 18621858]
22. Krishnamurthy G, Itoh A, Swanson JC, Bothe W, Karlsson M, Kuhl E, Miller DC, Ingels NB. Regional stiffening of the mitral valve anterior leaflet in the beating heart. Journal of Biomechanics. 2009; 42:2697–2701. [PubMed: 19766222]
23. Krishnamurthy G, Itoh A, Bothe W, Swanson J, Kuhl E, Karlsson M, Miller DC, Ingels NB. Stress-strain behavior of mitral valve leaflets in the beating ovine heart. Journal of Biomechanics. 2009; 42:1909–1916. [PubMed: 19535081]
24. Kunzelman KS, Cochran RP. Stress/strain characteristics of porcine mitral valve tissue: parallel versus perpendicular collagen orientation. Journal of Cardiac Surgery. 1992; 7:71–78. [PubMed: 1554980]

25. Kunzelman KS, Cochran RP, Chuong C, Ring WS, Verrier ED, Eberhart RD. Finite element analysis of the mitral valve. Journal of Heart Valve Disease. 1993; 2:326–340. [PubMed: 8269128]
26. Kunzelman KS, Cochran RP, Murphree SS, Ring WS, Verrier ED, Eberhart RC. Differential collagen distribution in the mitral valve and its influence on biomechanical behaviour. Journal of Heart Valve Disease. 1993; 2:236–244. [PubMed: 8261162]
27. Kunzelman KS, Reimink MS, Cochran RP. Annular dilatation increases stress in the mitral valve and delays coaptation: a finite element computer model. Cardiovascular Surgery. 1997; 5:427–434. [PubMed: 9350801]
28. Kunzelman KS, Quick DW, Cochran RP. Altered collagen concentration in mitral valve leaflets: biochemical and finite element analysis. Annals of Thoracic Surgery. 1998; 66:S198–S205. [PubMed: 9930448]
29. Kvitting JP, Bothe W, Göktepe S, Rausch MK, Swanson JC, Kuhl E, Ingels NB, Miller DC. Anterior mitral leaflet curvature during the cardiac cycle in the normal ovine heart. Circulation. 2010; 122:1683–1689. [PubMed: 20937973]
30. Liao J, Yang L, Grashow JS, Sacks MS. The relation between collagen fibril kinematics and mechanical properties of the mitral valve anterior leaflet. Journal of Biomechanical Engineering. 2007; 129:78–87. [PubMed: 17227101]
31. Maisano F, Redaelli A, Pennati G, Fumero R, Torracca L, Alfieri O. The hemodynamic effects of double-orifice valve repair for mitral regurgitation: a 3D computational model. European Journal of Cardiothoracic Surgery. 1999; 15:419–425. [PubMed: 10371115]
32. Maisano F, Redaelli A, Soncini M, Votta E, Arcobaso L, Alfieri O. An annular prosthesis for the treatment of functional mitral regurgitation: finite element model analysis of a dog bone-shaped ring prosthesis. Annals of Thoracic Surgery. 2005; 79:1268–1275. [PubMed: 15797061]
33. May-Newman K, Yin FC. Biaxial mechanical behavior of excised porcine mitral valve leaflets. American Journal of Physiology. 1995; 269:H1319–H1327. [PubMed: 7485564]
34. May-Newman K, Yin FC. A constitutive law for mitral valve tissue. Journal of Biomechanical Engineering. 1998; 120:38–47. [PubMed: 9675679]
35. Mulholland DL, Gotlieb AI. Cardiac valve interstitial cells: Regulator of valve structure and function. Cardiovascular Pathology. 1997; 6:167–174.
36. Nordrum IS, Skallerud B. Smooth muscle in the human mitral valve: extent and implications for dynamic modelling. Acta Pathologica, Microbiologica et Immunologica Scandinavica. 2012; 120:484–494.
37. Opie, LH. Heart Physiology: From Cell to Circulation. Pennsylvania: Lippincott Williams & Wilkins; 2003.
38. Padala M, Hutchison RA, Croft LR, Jimenez JH, Gorman RC, Gorman JH, Sacks MS, Yoganathan AP. Saddle shape of the mitral annulus reduces systolic strains on the P2 segment of the posterior mitral leaflet. Annals of Thoracic Surgery. 2009; 88:1499–1504. [PubMed: 19853100]
39. Pouch AM, Xu C, Yushkevich P, Jassar AS, Vergnat M, Gorman JH, Gorman RC, Jackson BM. Semi-automated mitral valve morphometry and computational stress analysis using 3D ultrasound. Journal of Biomechanics. 2012; 45:903–907. [PubMed: 22281408]
40. Prot V, Skallerud B, Holzapfel GA. Transversely isotropic membrane shells with application to mitral valve mechanics. Constitutive modeling and finite element implementation. International Journal for Numerical Methods in Engineering. 2007; 71:987–1008.
41. Prot V, Haaverstad R, Skallerud B. Finite element analysis of the mitral apparatus: annulus shape effect and chordal force distribution. Biomechanics and Modeling in Mechanobiology. 2009; 8:43–55. [PubMed: 18193309]
42. Prot V, Skallerud B. Nonlinear solid finite element analysis of mitral valves with heterogeneous leaflet layers. Computational Mechanics. 2009; 43:353368.
43. Rabbah JP, Saikrishnan N, Yoganathan AP. A novel left heart simulator for the multi-modality characterization of native mitral valve geometry and fluid mechanics. Annals of Biomedical Engineering.

44. Rausch MK, Bothe W, Kvitting JPE, Göktepe S, Miller DC, Kuhl E. In vivo dynamic strains of the ovine anterior mitral valve leaflet. Journal of Biomechanics. 2011; 44:1149–1157. [PubMed: 21306716]
45. Rausch MK, Bothe W, Kvitting JPE, Swanson JC, Ingels NB, Miller DC, Kuhl E. Characterization of mitral valve annular dynamics in the beating heart. Annals of Biomedical Engineering. 2011; 39:1690–1702. [PubMed: 21336803]
46. Rausch MK, Bothe W, Kvitting JP, Swanson JC, Miller DC, Kuhl E. Mitral valve annuloplasty - A quantitative clinical and mechanical comparison of different annuloplasty devices. Annals of Biomedical Engineering. 2012; 40:750–761. [PubMed: 22037916]
47. Rausch MK, Tibayan FA, Miller DC, Kuhl E. Evidence of adaptive mitral leaflet growth. Journal of the Mechanical Behavior of Biomedical Materials. 2012; 15:208–217. [PubMed: 23159489]
48. Rausch MK, Kuhl E. On the effect of prestrain and residual stress in thin biological membranes. submitted for publication. 2013
49. Reimink MS, Kunzelman KS, Verrier ED, Cochran RP. The effect of anterior chordal replacement on mitral valve function and stresses. A finite element study. American Society of Artificial Internal Organs. 1995; 41:M754–M762.
50. Salgo IS, Gorman JH, Gorman RC, Jackson BM, Bowen FW, Plappert T, St John Sutton MG, Edmunds LH Jr. Effect of annular shape on leaflet curvature in reducing mitral leaflet stress. Circulation. 2002; 106:711–717. [PubMed: 12163432]
51. Sacks MS, He Z, Baijens L, Wanant S, Shah P, Sugimoto H, Yoganathan AP. Surface strains in the anterior leaflet of the functioning mitral valve. Annals of Biomedical Engineering. 2002; 30:78–87.
52. Sacks MS, Enomoto Y, Graybill JR, Merryman WD, Zeeshan A, Yoganathan AP, Levy RJ, Gorman RC, Gorman JH. In-vivo dynamic deformation of the mitral valve anterior leaflet. Annals of Thoracic Surgery. 2006; 82:1369–1377. [PubMed: 16996935]
53. Sacks MS, Yoganathan AP. Heart valve function: a biomechanical perspective. Philosophical Transactions of the Royal Society of London B. 2007; 362:1369–1391.
54. Siefert AW, Jimenez JH, West DS, Koomalsingh KJ, Gorman RC, Gorman JH, Yoganathan AP. In-vivo transducer to measure dynamic mitral annular forces. Journal of Biomechanics. 2012; 45:1514–1516. [PubMed: 22483226]
55. Skallerud B, Prot V, Nordrum IS. Modeling active muscle contraction in mitral valve leaflets during systole: a first approach. Biomechanics and Modeling in Mechanobiology. 2011; 10:11–26. [PubMed: 20419330]
56. Taylor MT, Batten P, Brand NJ, Thomas PS, Yacoub MH. The cardiac valve interstitial cell. International Journal of Biochemistry & Cell Biology. 2003; 35:113–118. [PubMed: 12479860]
57. van Vlimmeren MAA, Driessen-Mol A, Oomens CWJ, Baaijens FPT. Passive and active contributions to generated force and retraction in heart valve tissue engineering. Biomechanics and Modeling in Mechanobiology. 2012; 11:1015–1027. [PubMed: 22246054]
58. Votta E, Maisano F, Soncini M, Redaelli A, Montevecchi FM, Alfieri O. 3-D computational analysis of the stress distribution on the leaflets after edge-to-edge repair of mitral regurgitation. Journal of Heart Valve Disease. 2002; 11:810–822. [PubMed: 12479282]
59. Votta E, Maisano F, Bolling SF, Alfieri O, Montevecchi FM, Redaelli A. The Geoform disease-specific annuloplasty system. Annals of Thoracic Surgery. 2007; 84:92–101. [PubMed: 17588392]
60. Weinberg EJ, Kaazempur-Mofrad MR. A finite shell element for heart mitral valve leaflet mechanics, with large deformations and 3D constitutive material model. Journal of Biomechanics. 2006; 40:705–711. [PubMed: 16574127]
61. Xu C, Brinster CJ, Jassar AS, Vergnat M, Eperjesi TJ, Gorman RC, Gorman JH, Jackson BM. A novel approach to in vivo mitral valve stress analysis. American Journal of Physiology - Heart and Circulatory Physiology. 2010; 299:H1790–H1794. [PubMed: 20952665]

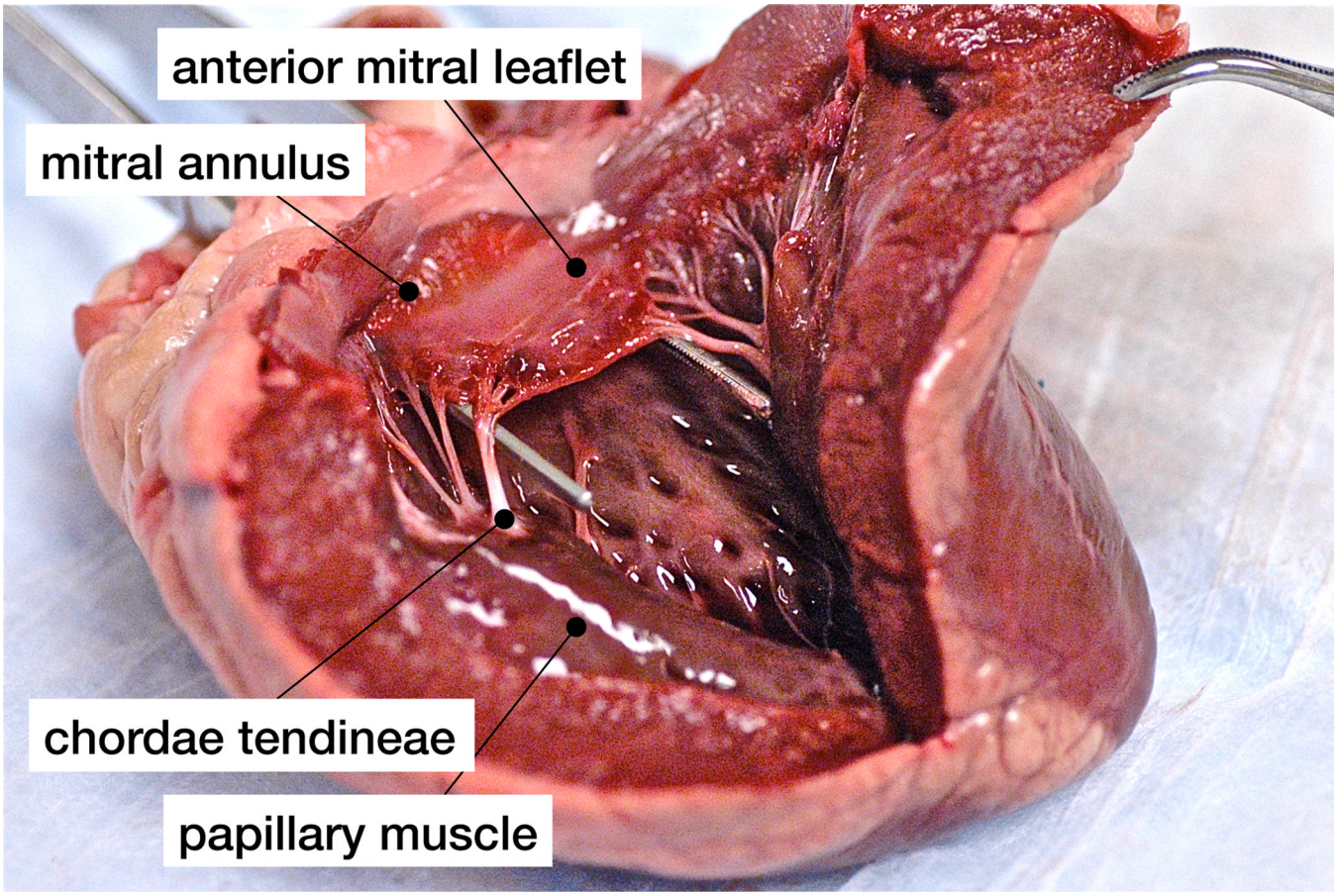

Fig. 1.
The mitral valve apparatus consists of three elements: the mitral leaflets, the mitral annulus, and the subvalvular apparatus including the chordae tendineae and the papillary muscles. This lateral left ventricular view shows the atrial surface of the anterior mitral leaflet, attached through the mitral annulus, and supported by the chordae tendineae.

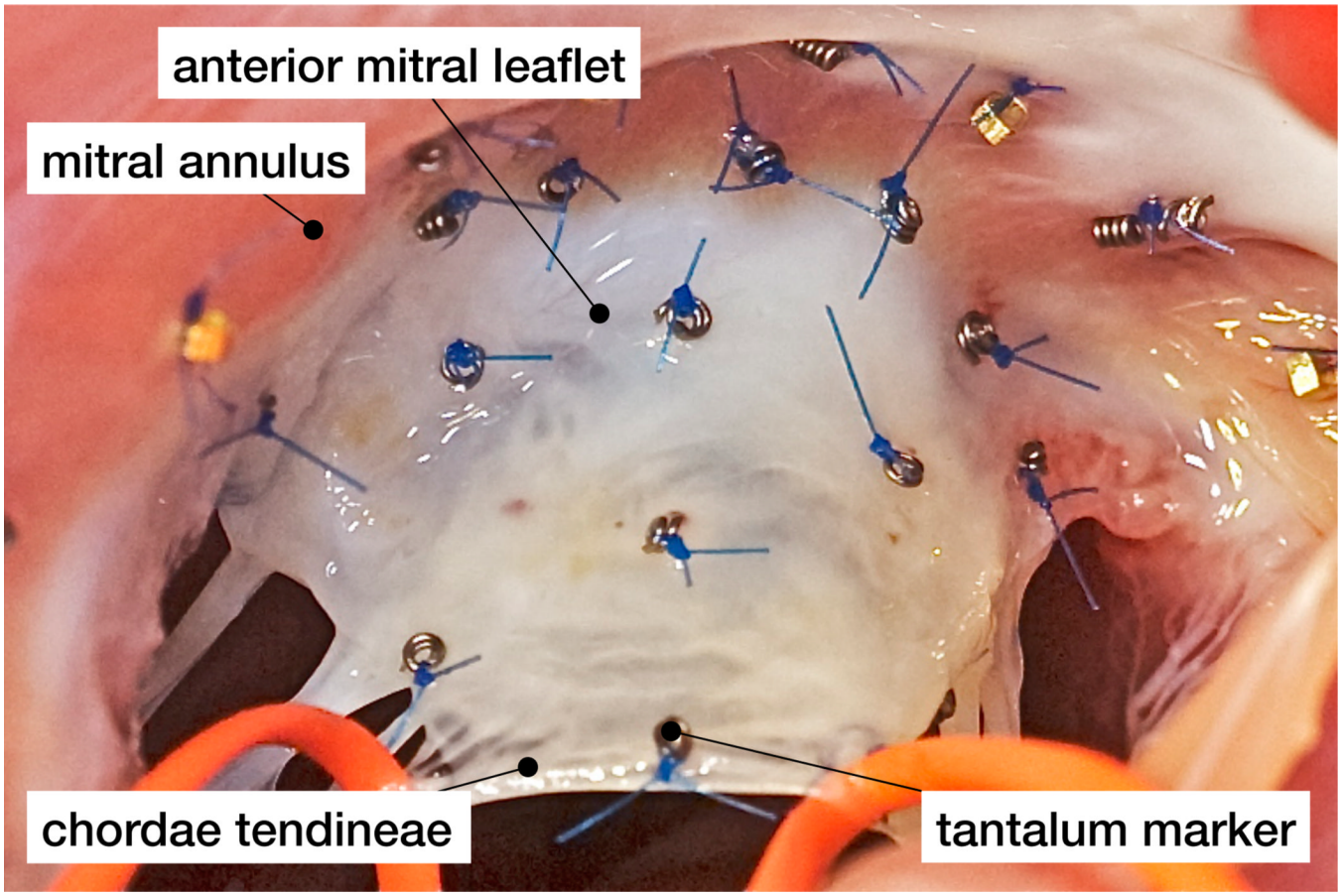

Fig. 2.
Intraoperative photograph of mitral annulus and anterior mitral leaflet with implanted marker array to reconstruct the leaflet deformation field in vivo.

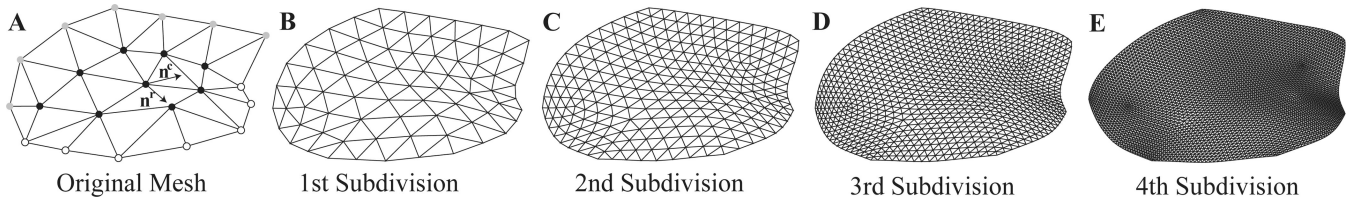

Fig. 3.

A) Original triangular discretization with 30 triangular shell elements based on in vivo belly marker coordinates (black spheres), annular marker coordinates (grey spheres), and free edge marker coordinates (white spheres). Circumferential direction ($\boldsymbol{n}^{c}$) and radial direction ($\boldsymbol{n}^{r}$) are indicated by arrows. B–E) Four levels of refinement created using a custom-designed subdivision algorithm with 120, 480, 1920, and 7680 triangular shell elements.

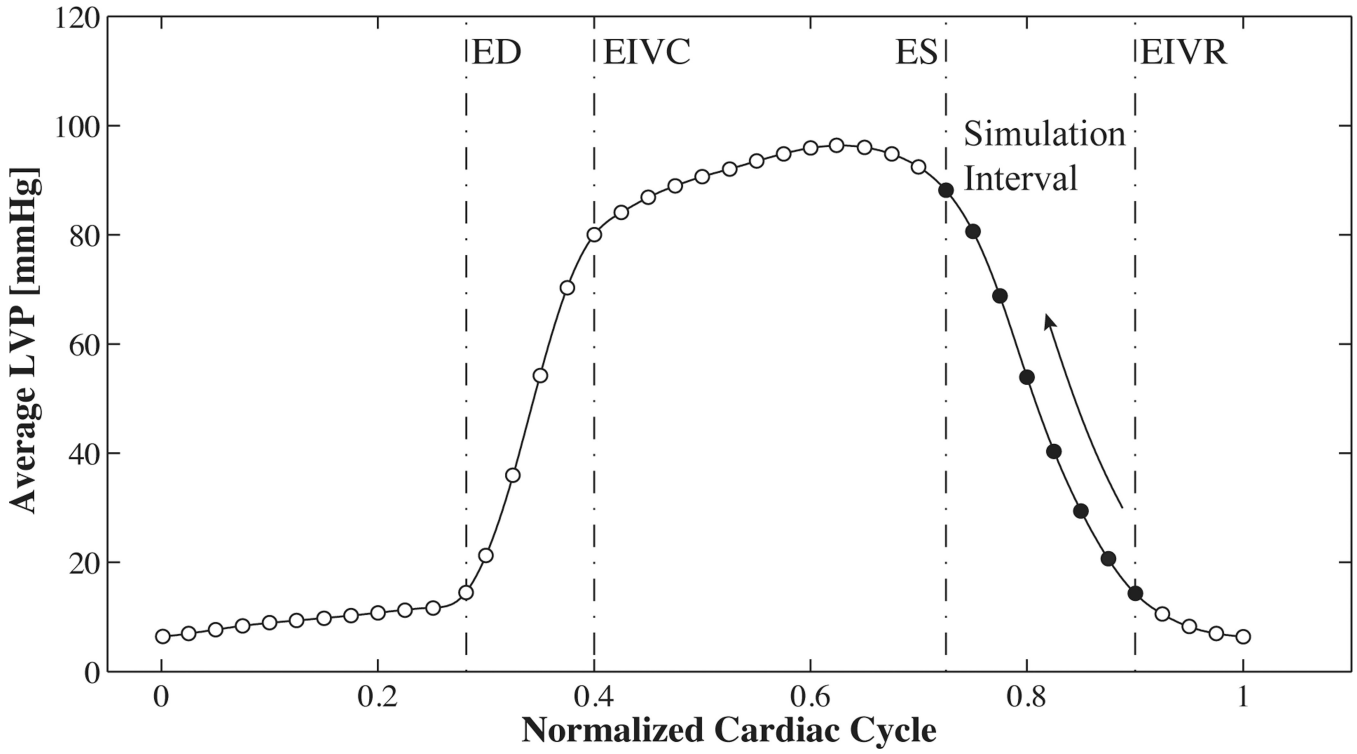

Fig. 4.

Left ventricular pressure curve averaged over all 57 animals. Shown are the time intervals between end-diastole (ED), end-isovolumic contraction (EIVC), end-systole (ES), end-isovolumic relaxation (EIVR), and end-diastole (ED) of the next beat. Filled circles indicate the eight discrete time steps within the simulation interval. The arrow indicates the direction of the simulation.

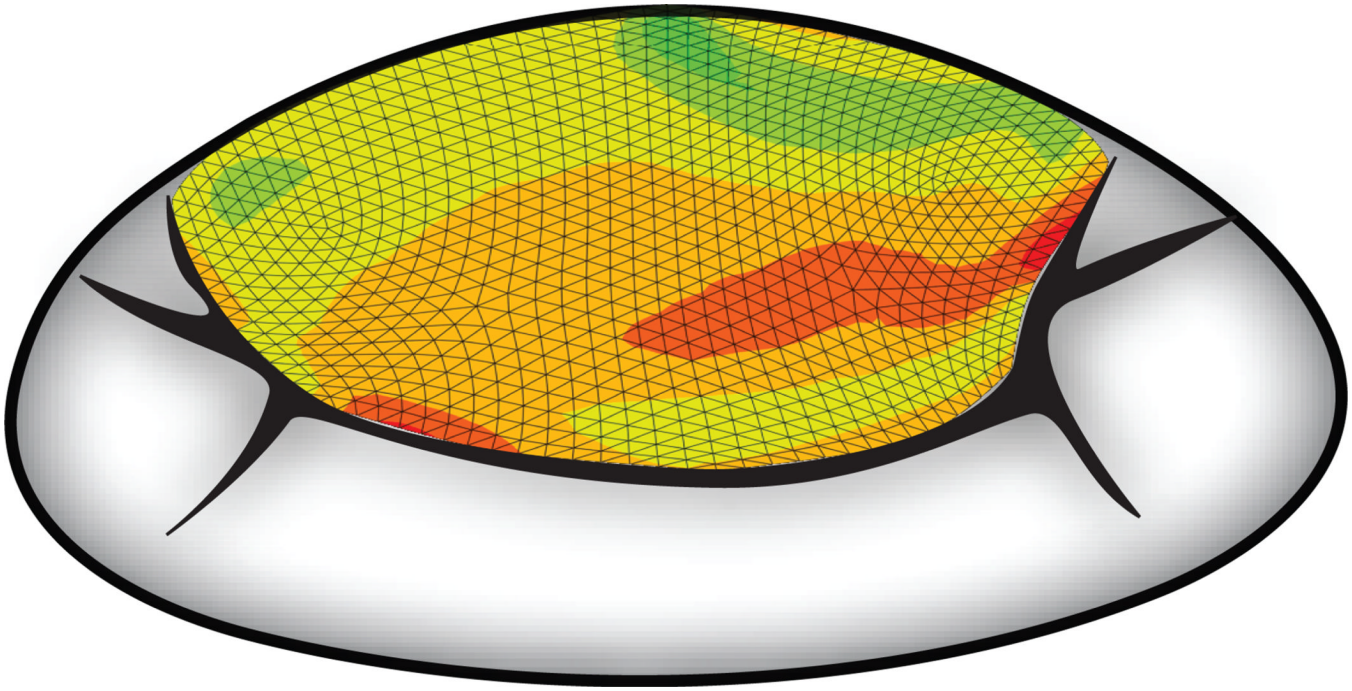

Fig. 5.
Finite element discretization of the anterior mitral leaflet discretized with 1920 triangular shell elements and 1017 nodes, embedded in the mitral valve complex.

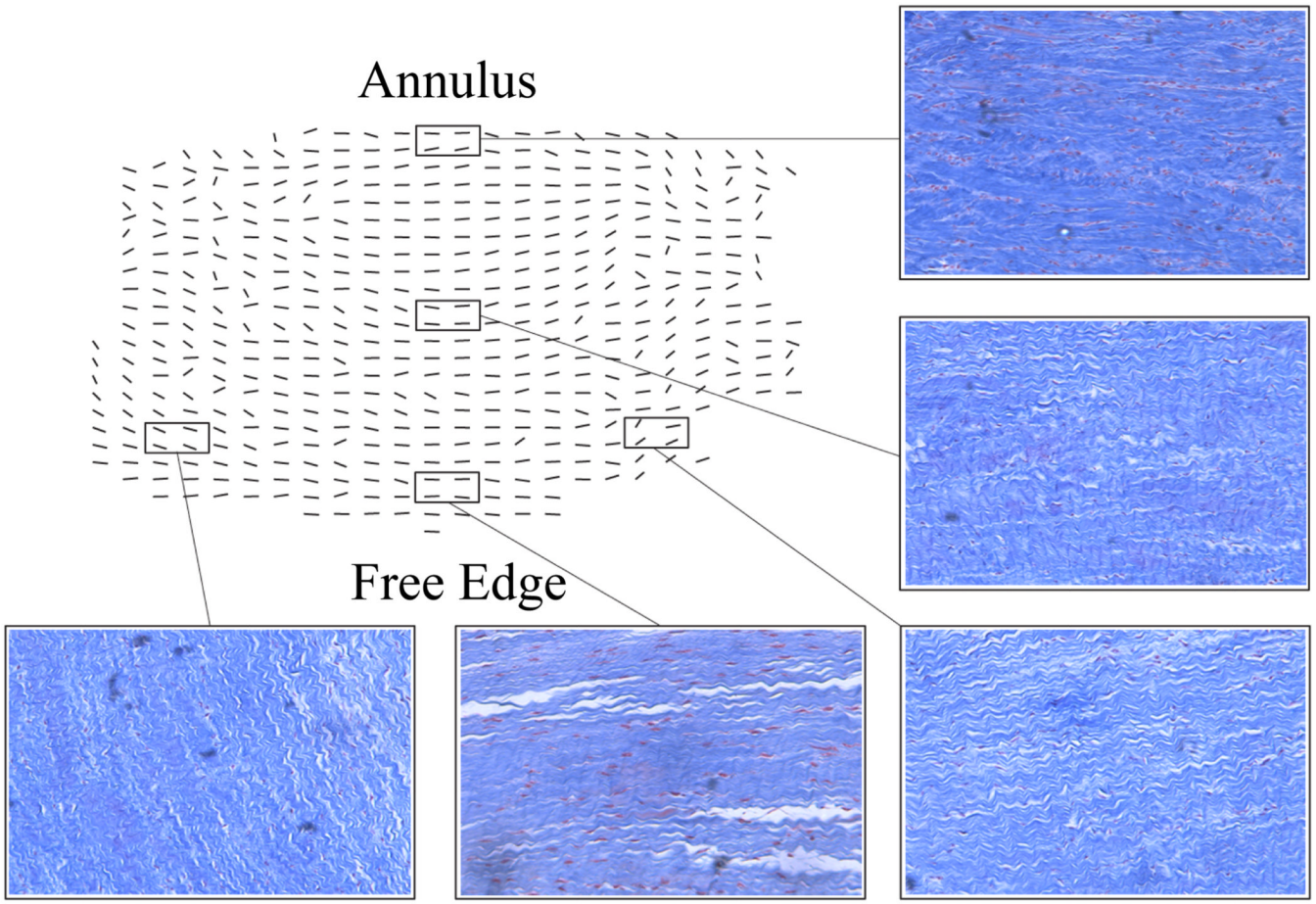

Fig. 6.

Collagen fiber orientation across a representative ovine anterior mitral leaflet after staining with Masson's trichrome. Collagen fibers are stained blue. Fiber orientations are extracted semi-manually from microscopic images.

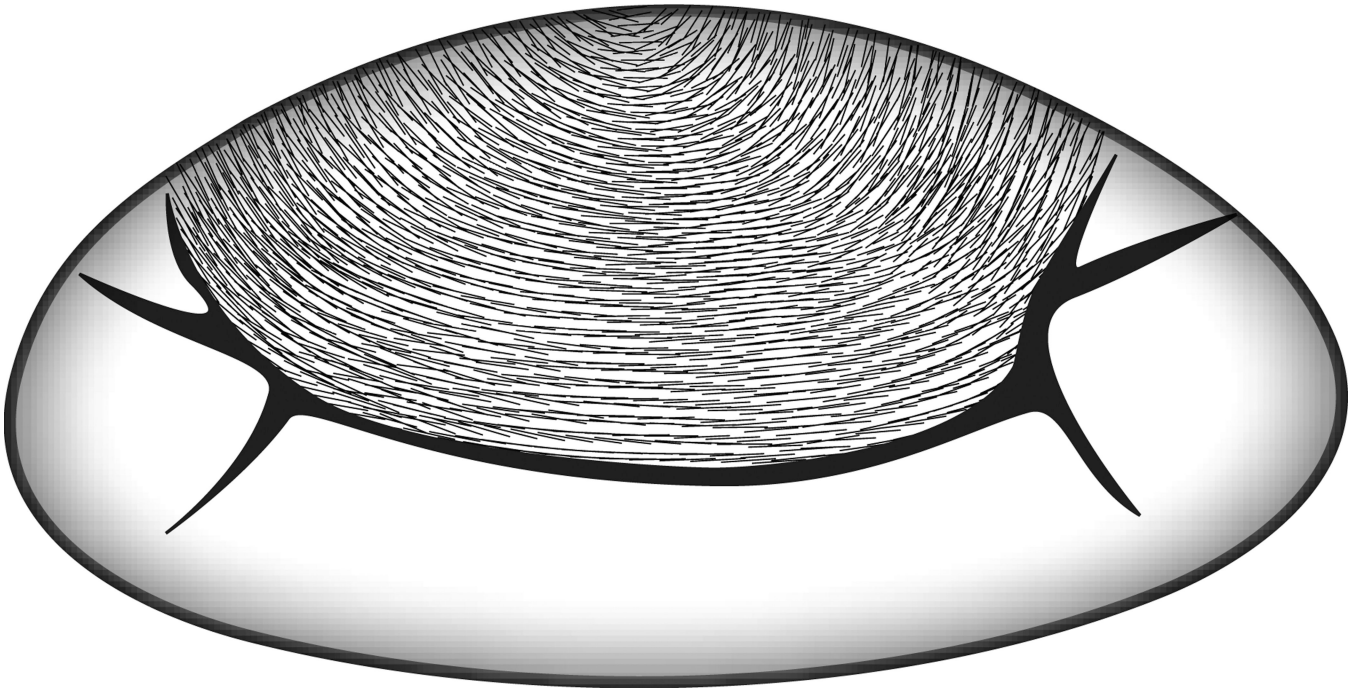

Fig. 7.
Collagen fiber orientation in the computational model of the anterior mitral leaflet created from small angle light scattering data and histological studies in our laboratory.

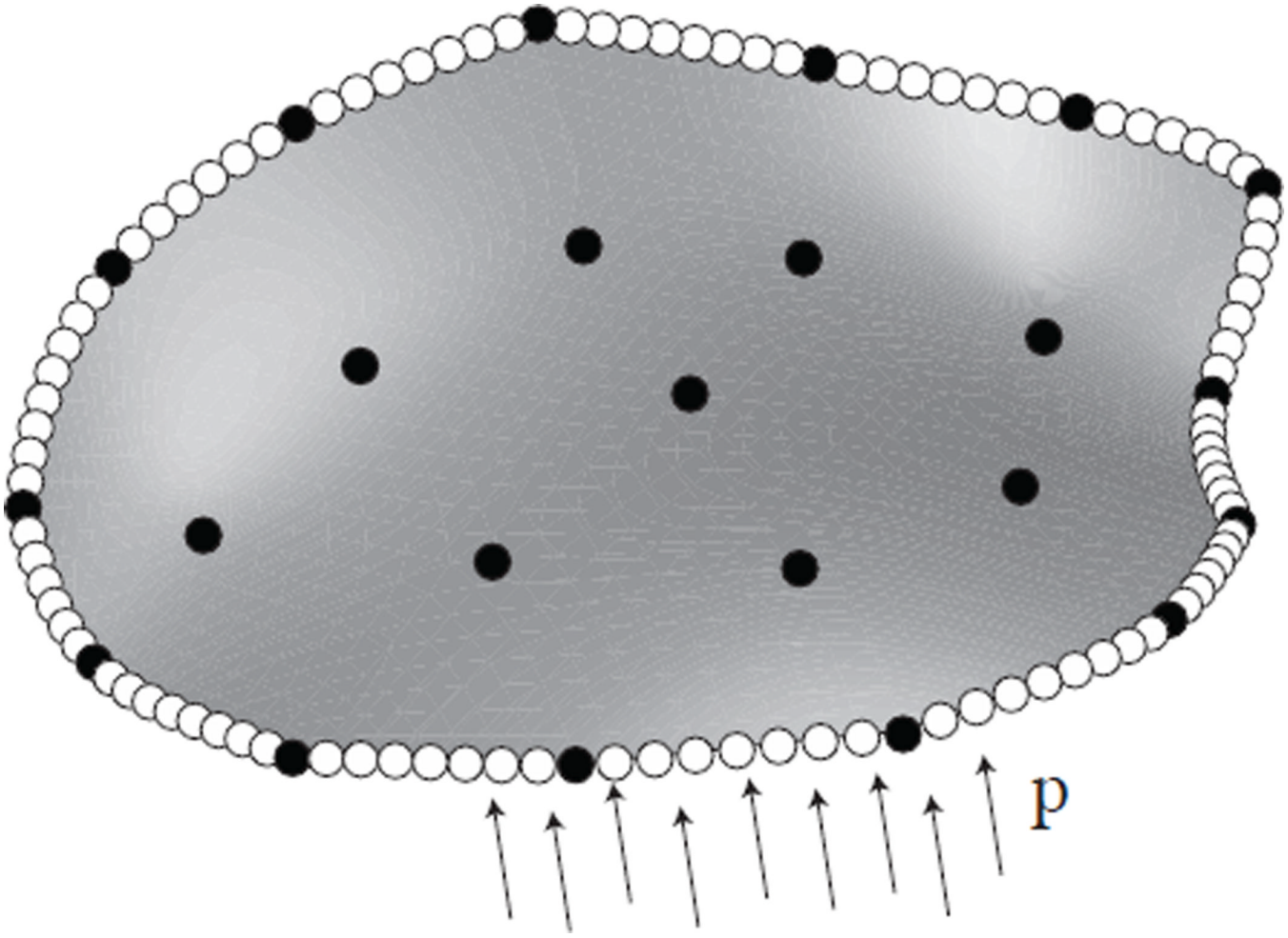

Fig. 8.

Finite element model of the mitral leaflet. The leaflet boundary with assigned inhomogeneous Dirichlet boundary conditions is indicated by white spheres; the original marker locations are indicated by black spheres. We assigned the transvalvular pressure *p*, derived from micromanomater pressure readings in the left ventricle and the left atrium, to the ventricular surface of the mitral leaflet as indicated by the black arrows.

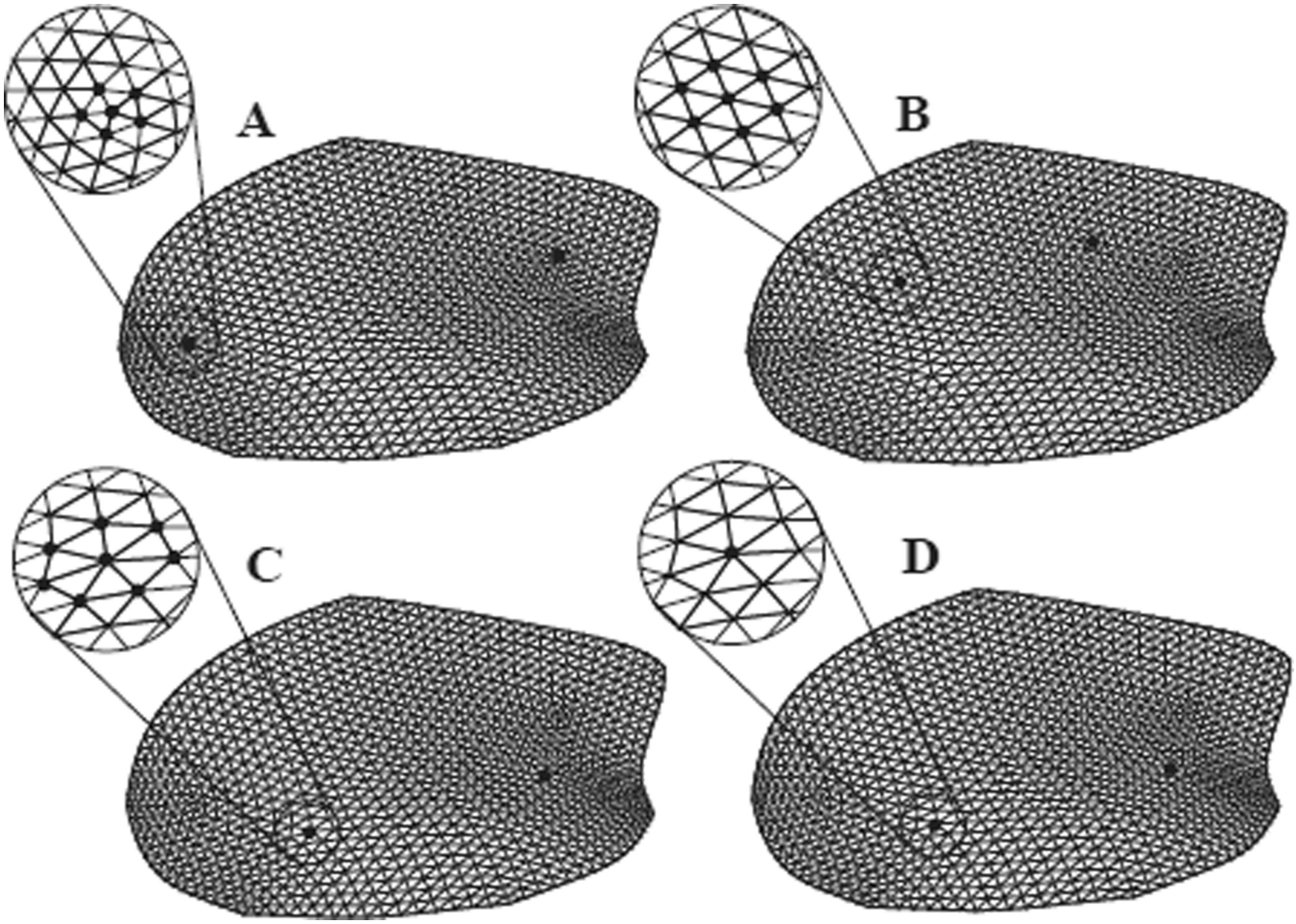

Fig. 9.

Sensitivity study for varying chordae insertion sites. A) Chordae insert close to the annulus and the anterior and posterior commissures. B) Chordae insert close to the annulus and close the midline of the anterior leaflet. C) Chordae insert closer to the free edge. D) A single cord inserts closer to the free edge. All chordae are connected to the corresponding papillary muscle tips.

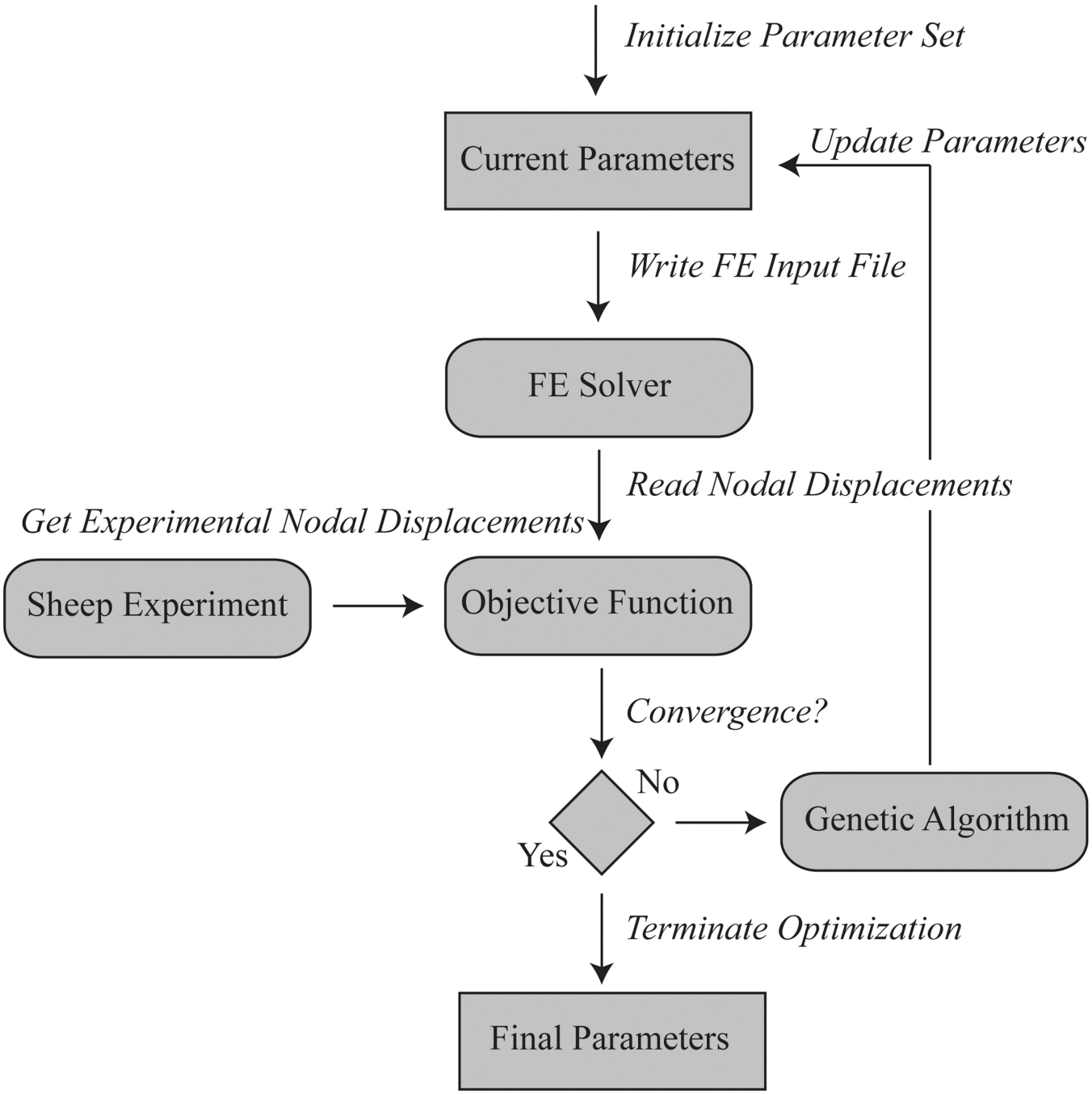

Fig. 10.
Flow chart of inverse finite element analysis for systematic parameter identification. For each parameter set, we run a simulation and evaluate the average nodal displacement error e as objective function. Until the algorithm has converged, we iteratively refine the parameter set using a genetic algorithm and rerun the analysis.

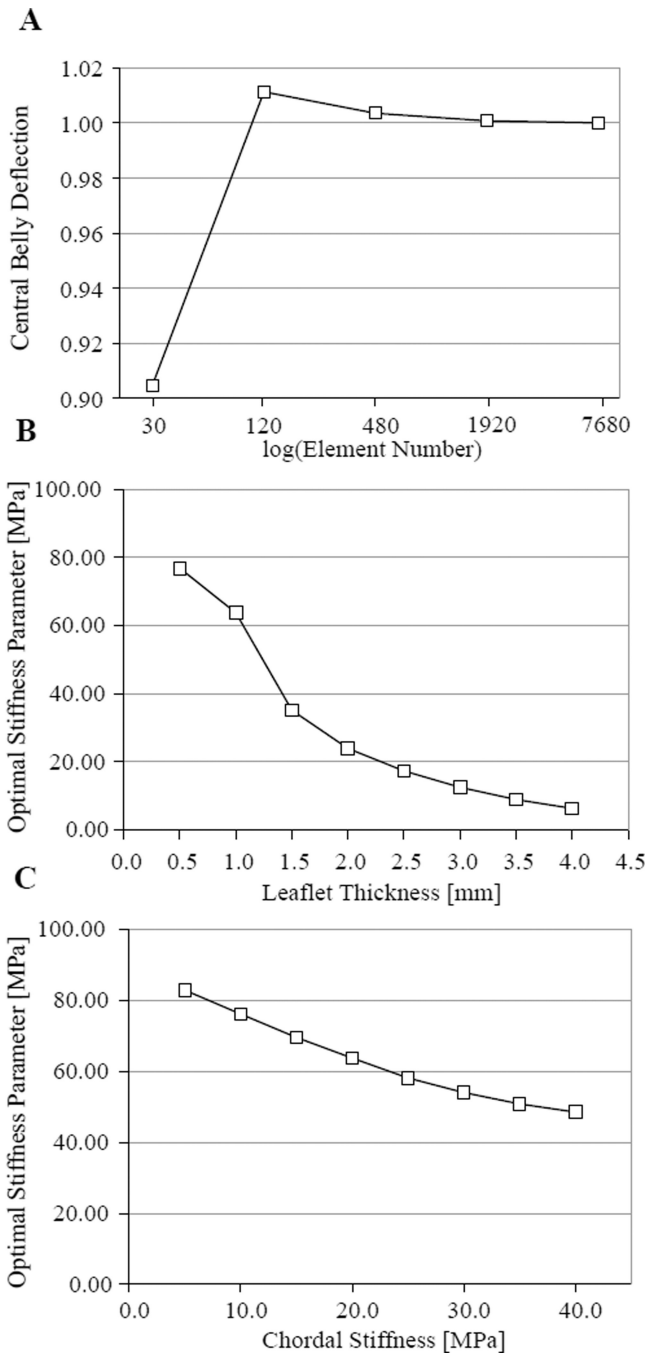

Fig. 11.

Sensitivity analyses for isotropic model. A) Sensitivity of central belly deflection with varying mesh densities. B) Sensitivity of the optimal stiffness parameter c_0 with varying leaflet thicknesses.

C) Sensitivity of the optimal stiffness parameter c_0 with varying chordae stiffnesses.

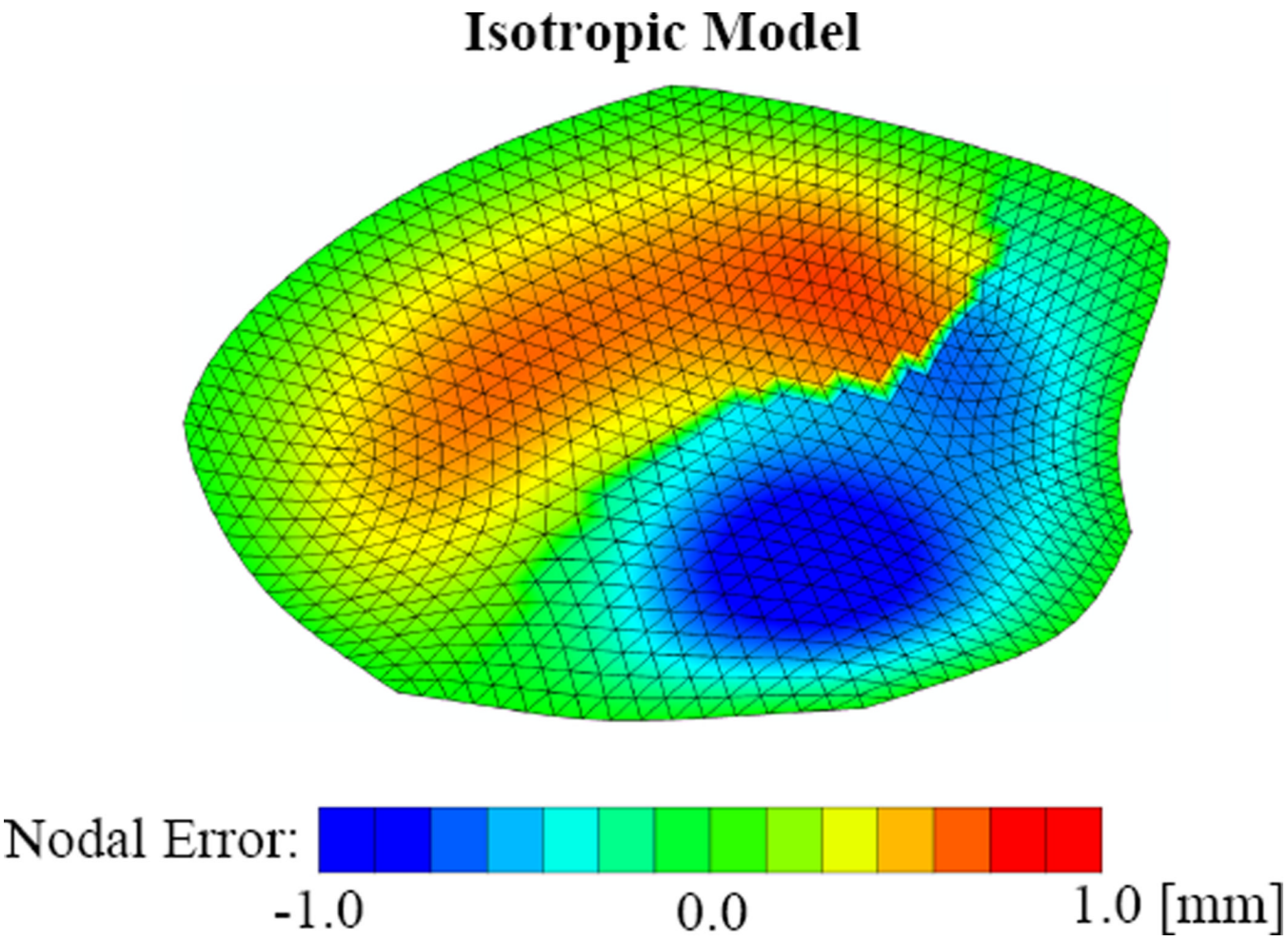

Fig. 12.

Regional variation of displacement error for isotropic model with homogeneous leaflet thickness. Positive errors, illustrated in red, indicate that the experimental leaflet moved less far into the atrium than the simulated leaflet. Negative errors, illustrated in blue, indicate that the experimental leaflet moved farther into the atrium than the simulated leaflet.

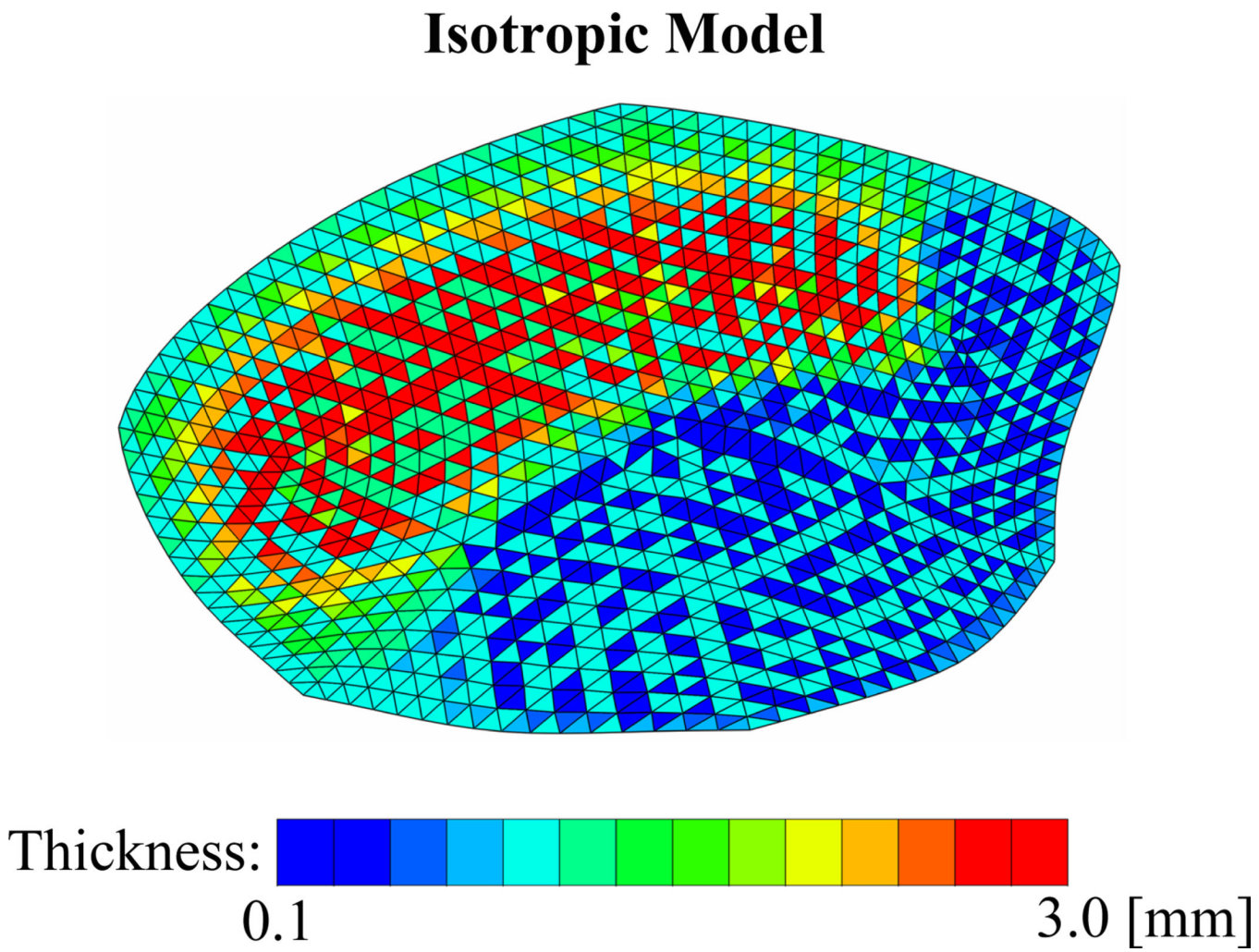

Fig. 13.
Optimized leaflet thickness for isotropic model. Regions close to the annulus, illustrated in red, display a maximum leaflet thickness of 3.0mm. Regions around the leaflet belly and close to the free edge, illustrated in blue, display a minimum leaflet thickness of 0.1mm.

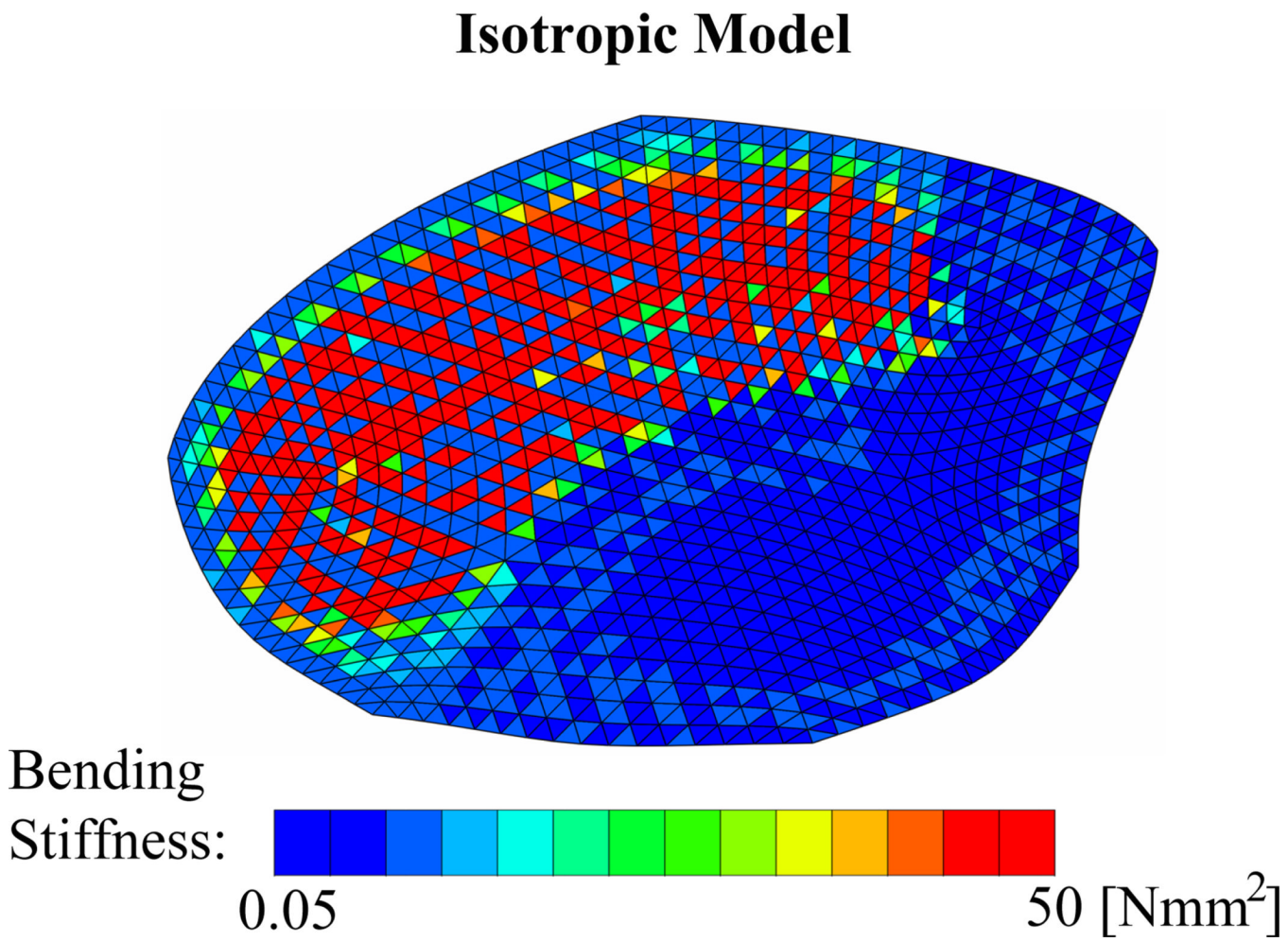

Fig. 14.

Optimized bending stiffness for isotropic model. Regions close to the annulus, illustrated in red, display a maximum bending stiffness of 50Nmm^2. Regions around the leaflet belly and close to the free edge, illustrated in blue, display a minimum bending stiffness of 0.05Nmm^2.

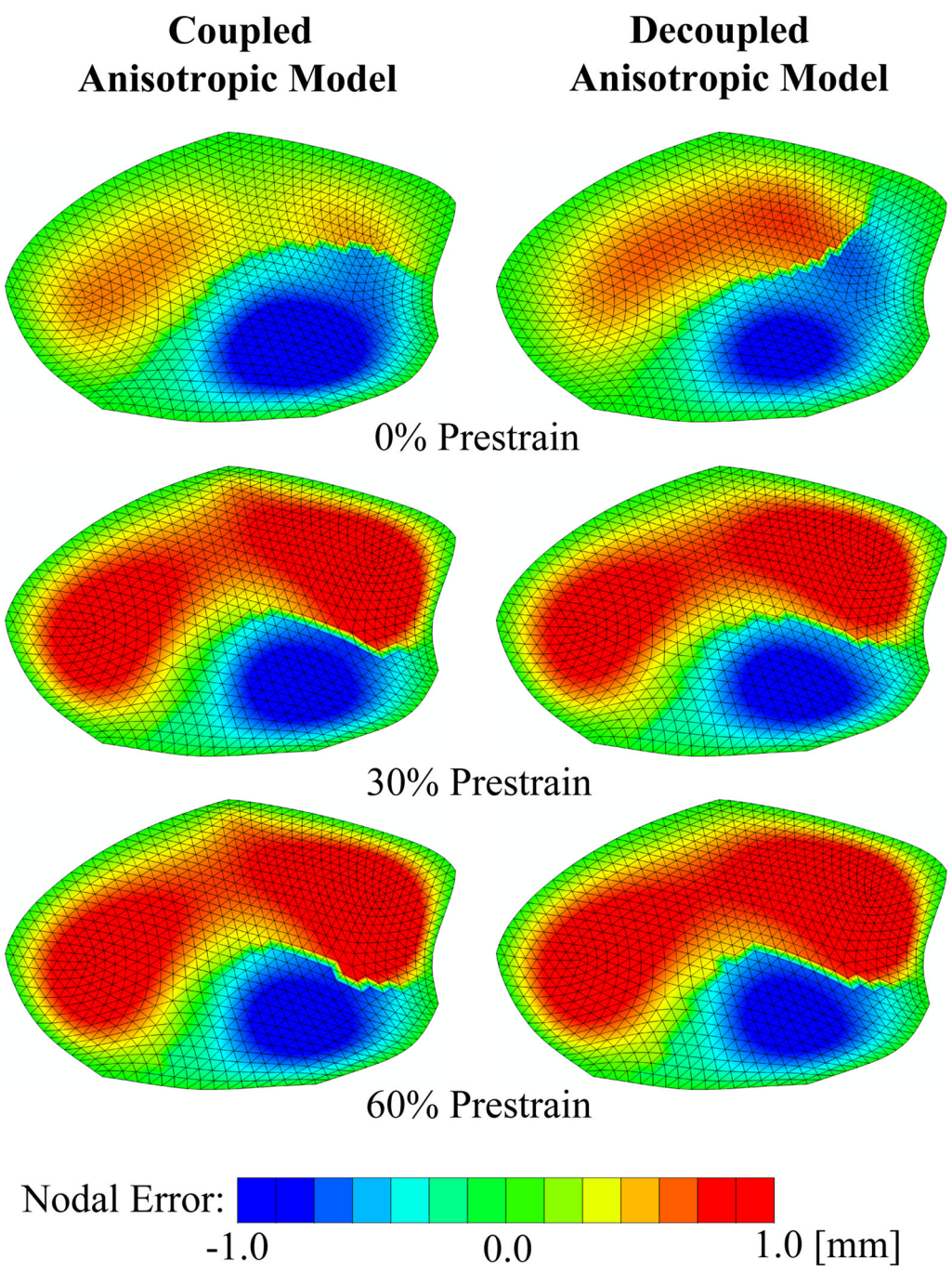

Fig. 15.

Regional displacement error for coupled and decoupled anisotropic models for three levels of prestrain. Positive errors, illustrated in red, indicate that the experimental leaflet moved less far into the atrium than the simulated leaflet. Negative errors, illustrated in blue, indicate that the experimental leaflet moved farther into the atrium than the simulated leaflet.

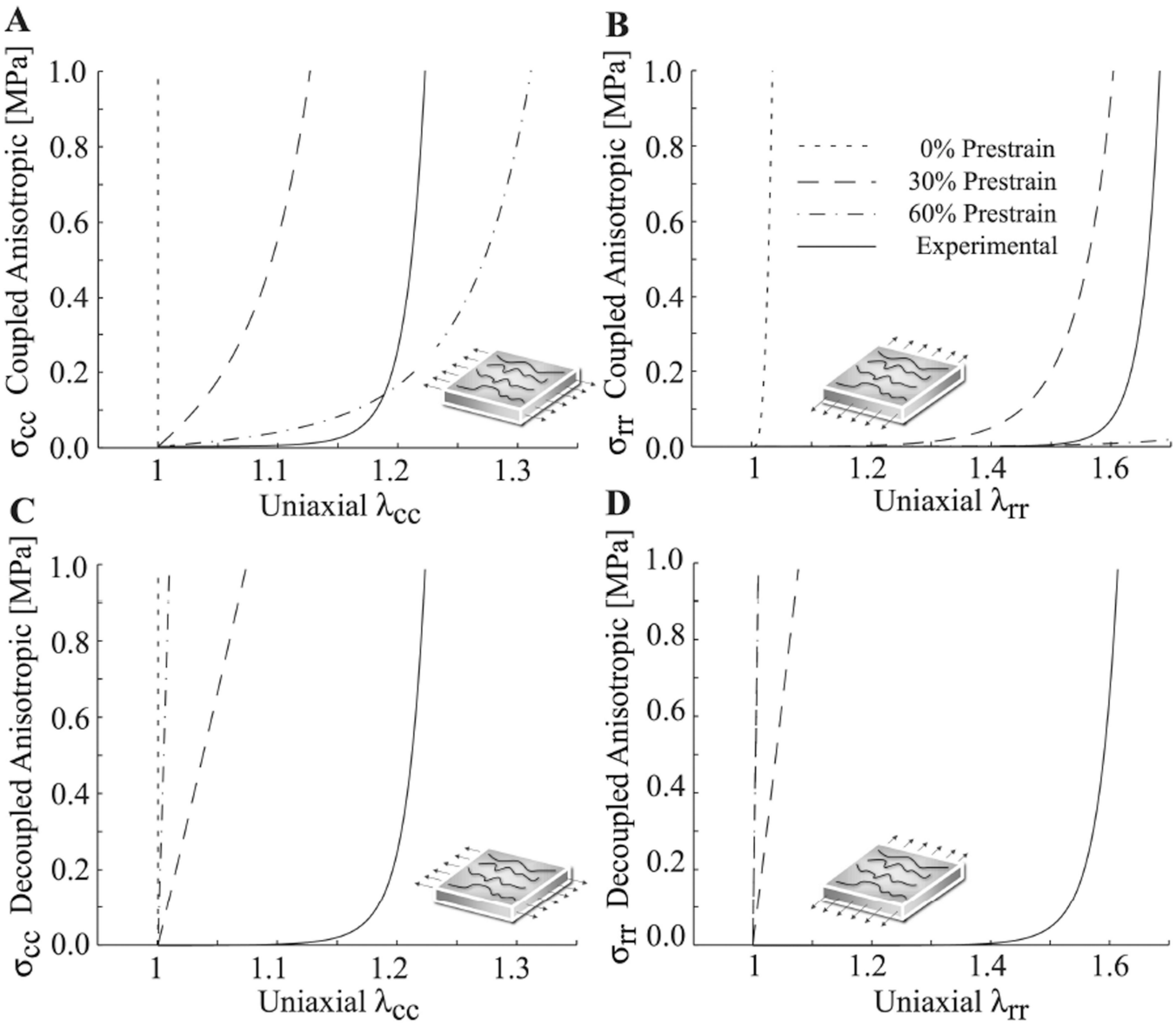

Fig. 16.

Stress-stretch responses for coupled and decoupled anisotropic models in a virtual uniaxial tensile test at three different levels of prestrain. For comparison, the solid line illustrates the coupled model fit to experimental ex vivo data [34]. A) Coupled model in circumferential direction. B) Coupled model in radial direction. C) Decoupled model in circumferential direction. D) Decoupled model in radial direction.

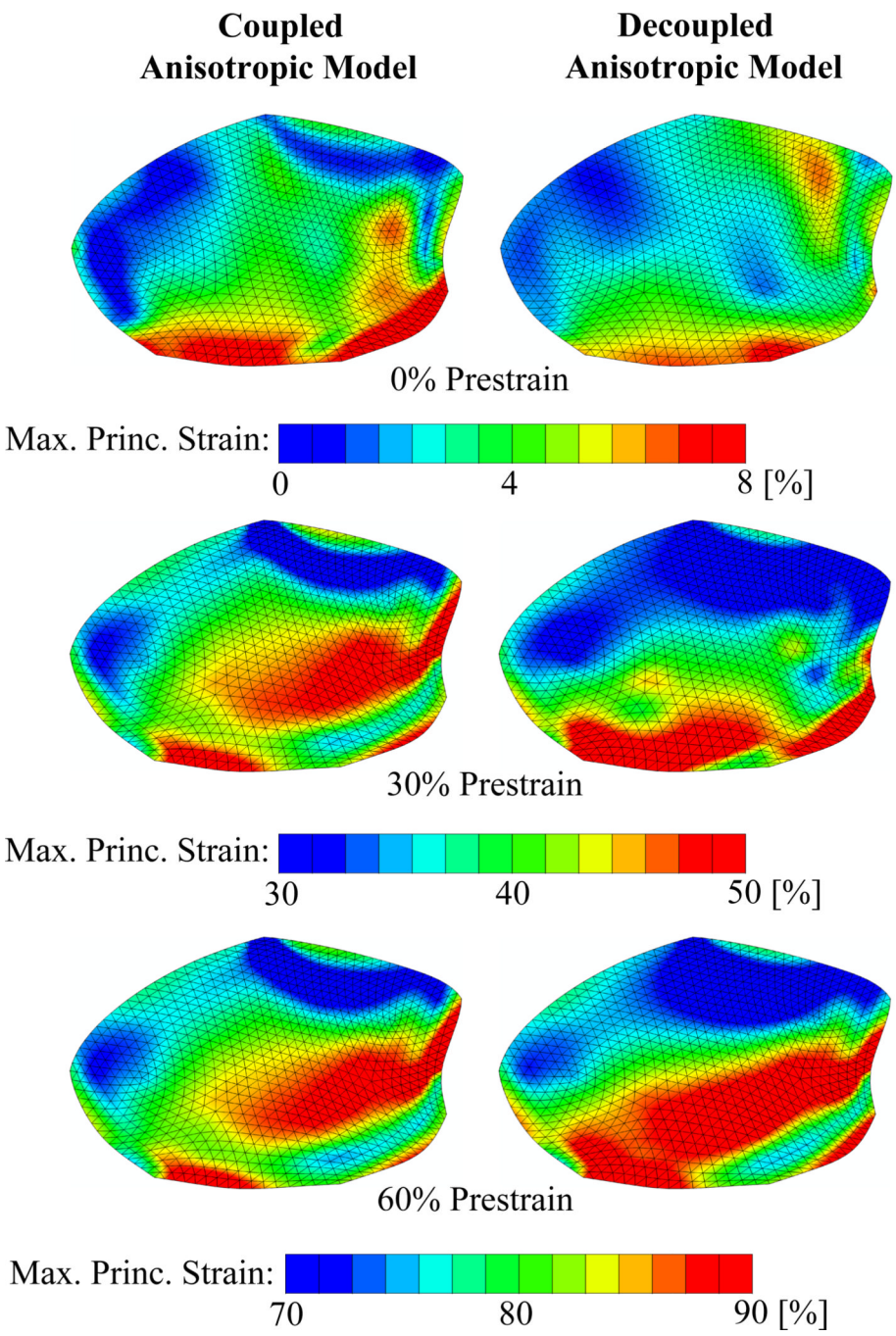

Fig. 17.

Maximum principal Green-Lagrange strains for coupled model and decoupled model for three levels of prestrain. Strains are evaluated between end-isometric relaxation and end-systole. With linearly increasing prestrain levels, the leaflet strain increases super-linearly due to the multiplicative effect of prestrain on leaflet strain.

Table 1

Average nodal displacement error for coupled and decoupled anisotropic models for three levels of prestrain.

	Coupled Anisotropic Model	Decoupled Anisotropic Model
prestrain [%]	**average nodal error *e* [mm]**	**average nodal error *e* [mm]**
0	0.5606	0.5052
30	0.5753	0.5286
60	0.5878	0.5701

Table 2

Material parameter values for coupled and decoupled anisotropic models for three levels of prestrain. Highlighted parameter set and * symbol indicate the model with the best overall fit, the coupled anisotropic model with 30% prestrain.

Coupled Anisotropic Model

prestrain [%]	c_0 [kPa]	c_1 [−]	c_2 [−]
0	119,020.7	152.4	185.5
30*	**35.9**	**2.3**	**9.8**
60	9.4	0.6	3.4

Decoupled Anisotropic Model

prestrain [%]	c_0 [kPa]	c_1 [kPa]	c_2 [−]	κ [−]
0	18,364.4	2,499,419.2	97.4	0.00
30	2,184.0	116.7	17.5	0.05
60	17,200.3	754.7	5.8	0.11